



HAL
open science

Clustering mesoscale convective systems with laser-based water vapor $\delta^{18}\text{O}$ monitoring in Niamey (Niger)

Guillaume Tremoy, Françoise Vimeux, Salifou Soumana, Ide Souley, Camille Risi, Guillaume Favreau, Monique Oï

► **To cite this version:**

Guillaume Tremoy, Françoise Vimeux, Salifou Soumana, Ide Souley, Camille Risi, et al.. Clustering mesoscale convective systems with laser-based water vapor $\delta^{18}\text{O}$ monitoring in Niamey (Niger). *Journal of Geophysical Research: Atmospheres*, 2014, 119 (9), pp.5079-5103. 10.1002/2013JD020968 . hal-01083039

HAL Id: hal-01083039

<https://polytechnique.hal.science/hal-01083039>

Submitted on 28 Oct 2020

HAL is a multi-disciplinary open access archive for the deposit and dissemination of scientific research documents, whether they are published or not. The documents may come from teaching and research institutions in France or abroad, or from public or private research centers.

L'archive ouverte pluridisciplinaire **HAL**, est destinée au dépôt et à la diffusion de documents scientifiques de niveau recherche, publiés ou non, émanant des établissements d'enseignement et de recherche français ou étrangers, des laboratoires publics ou privés.

RESEARCH ARTICLE

10.1002/2013JD020968

Key Points:

- Isotopic analyses on 74 Sahelian rain systems
- A classification into three types of water vapor isotopic composition evolution
- Box model is used to better evaluate dynamics versus rain evaporation processes

Correspondence to:

G. Tremoy,
Guillaume.Tremoy@lscce.ipsl.fr

Citation:

Tremoy, G., F. Vimeux, S. Soumana, I. Souley, C. Risi, G. Favreau, and M. Oï (2014), Clustering mesoscale convective systems with laser-based water vapor $\delta^{18}\text{O}$ monitoring in Niamey (Niger), *J. Geophys. Res. Atmos.*, 119, 5079–5103, doi:10.1002/2013JD020968.

Received 30 SEP 2013

Accepted 8 APR 2014

Accepted article online 12 APR 2014

Published online 6 MAY 2014

Clustering mesoscale convective systems with laser-based water vapor $\delta^{18}\text{O}$ monitoring in Niamey (Niger)

Guillaume Tremoy¹, Françoise Vimeux^{1,2}, Salifou Soumana³, Ide Souley³, Camille Risi⁴, Guillaume Favreau², and Monique Oï²

¹Institut Pierre Simon Laplace, Laboratoire des Sciences du Climat et de l'Environnement, UMR 8212 (CEA-CNRS-UVSQ), CE Saclay, Orme des Merisiers, Gif-sur-Yvette, France, ²Institut de Recherche pour le Développement, Laboratoire HydroSciences Montpellier, UMR 5569 (CNRS-IRD-UM1-UM2), Montpellier, France, ³Institut des Radiosotopes, Université Abdou Moumouni de Niamey, Niamey, Niger, ⁴Institut Pierre Simon Laplace, Laboratoire de Météorologie dynamique, (UPMC, CNRS), Paris, France

Abstract The isotopic composition of surface water vapor (δ_v) has been measured continuously in Niamey along with the isotopic composition of event-based precipitation (δ_p) since 2010. We investigate the evolution of water vapor and precipitation isotope ratios during rain events of the 2010, 2011, and 2012 monsoon periods. We establish a classification of rain systems into three types based on the δ_v temporal evolution. We find that 51% of rain events (class A) exhibit a sharp decrease in $\delta^{18}\text{O}_v$ in phase with the surface air temperature drop, leading to a depletion of water vapor by -1.9% on average during rainfall. Twenty-nine percent of rain events (class B) show a similar decrease in $\delta^{18}\text{O}_v$ in phase with the temperature drop but are characterized by a progressive enrichment of the vapor in the stratiform region, resulting in a depletion of water vapor by -1.2% on average during rainfall. The last 20% of the rain events (class C) are associated with a progressive increase in $\delta^{18}\text{O}_v$ during rainfall ($+0.8\%$). We also examine the temporal evolution of water vapor deuterium excess (d_v) which shows a sharp increase as $\delta^{18}\text{O}_v$ decreases, followed by a progressive decrease in the stratiform part for classes A and B. Using a basic box model, we examine for each class the respective roles that mesoscale subsidence and rain evaporation play on the evolution of $\delta^{18}\text{O}_v$. We show that those two processes are dominant for class A, whereas other processes may exert a major role on $\delta^{18}\text{O}_v$ for classes B and C.

1. Introduction

Water molecules are present in nature under different forms and abundances, namely, H_2^{16}O , H_2^{18}O , and HD^{16}O for the most abundant, since hydrogen and oxygen elements have several stable isotopes. They have different masses and symmetries that create differences in their physical properties (saturation vapor pressure, molecular diffusivity). Therefore, they are redistributed in the different water reservoirs (solid, liquid, vapor) during phase changes, due to equilibrium and kinetic processes.

A large number of physical processes can impact the isotopic composition of precipitation in the tropics [Risi *et al.*, 2008a, 2010; Vimeux *et al.*, 2011]. Among them, processes associated with atmospheric convection are known to play an important role [Gedzelman and Lawrence, 1990; Lawrence *et al.*, 2004]. It has been suggested from modeling studies that rain evaporation, diffusive exchanges, and advection of depleted vapor from unsaturated downdrafts are the primary controls on the isotopic composition of precipitation in convective environment [Bony *et al.*, 2008; Risi *et al.*, 2008b]. Recently, Kurita [2013] used shipboard observations to study the isotopic response of water vapor and precipitation to mesoscale convective systems (hereafter MCS) over the ocean. He suggested that the amount effect reflects the development of a precipitation system from an isolated to a large-scale system and that past large-scale convective activity can be reconstructed from isotope records. Monitoring the isotopic composition of precipitation and water vapor may provide better constraints on the processes related to atmospheric convection.

Atmospheric convection exhibits different types, ranging from isolated convection to well-organized convective systems, from shallow to deep convection. In the Sahel region, much of the rain is produced by organized MCS such as squall lines [Mathon *et al.*, 2002] which propagates westward over West Africa. The dynamical structure and microphysical processes involved in MCS are well documented through several observational [Zipser, 1977; Chong *et al.*, 1987; Chalon *et al.*, 1988; Hauser *et al.*, 1988; Chong and Hauser, 1989;

Houze, 2004] and numerical studies [Lafore *et al.*, 1988; Redelsperger and Lafore, 1988; Lafore and Moncrieff, 1989]. The convective part of MCS is associated with strong updrafts and convective subsidence, whereas the stratiform part is mainly associated with mesoscale subsidence combined with a dry rear-to-front flow. Partial reevaporation of falling droplets in unsaturated downdrafts induces a cooling of air which spreads as a density current (also called cold pool) at the surface [Charba, 1974; Liu and Moncrieff, 1996; Moncrieff and Liu, 1999]. Rain evaporation is usually higher in the stratiform zone [Zahiri, 2007]. However, the amount of rain that is reevaporated is difficult to constrain precisely.

The isotopic composition of precipitation exhibits a robust evolution along squall lines [Taupin and Gallaire, 1998]. Recently, Risi *et al.* [2010] confirmed this feature and suggested that (1) precipitation reequilibrates isotopically as it falls and (2) processes controlling the isotopic composition of water vapor also control the isotopic composition of precipitation. This modeling approach suggests that the main factors controlling the isotopic evolution are squall line dynamics, especially mesoscale subsidence of depleted air at the rear of the squall line, and rain reevaporation [Risi *et al.*, 2010]. However, there was no any observation available in the water vapor phase to validate the results. This highlighted the need for new water vapor observations in tropical regions where deep convection and rain evaporation are important, like in the Sahel.

Actually, water vapor isotopic measurements are useful for answering remaining questions: Does water vapor evolve in the same way along different rain systems? What are the dominant processes affecting the isotopic composition of water vapor? What is the degree of equilibration between raindrops and the low-level water vapor? Does rain evaporation have a strong isotopic signature on the cold pool water vapor? If so, is it possible to quantify the proportion of atmospheric moisture which originates from rain reevaporation of falling droplets and subsiding dehydrated air from higher vertical level?

Indeed, the isotopic composition of water vapor provides information on processes governing moisture budget that is not available from humidity measurements alone or by the isotopic composition of precipitation. Since each process is expected to have a specific isotopic signature [Noone, 2012], changes in water vapor isotope ratios relative to humidity can help isolate the dominant processes of the atmospheric water cycle. The importance of rain evaporation and that of dehydration in the tropical midtroposphere in the budget of lower tropospheric humidity have been illustrated from the Tropospheric Emission Spectrometer satellite humidity/isotopes data [Worden *et al.*, 2007]. Instrumental devices based on spectroscopic detection in the infrared region also provide such simultaneous in situ measurements at high frequency [Kerstel *et al.*, 1999]. These new techniques offer the possibility to investigate the mixing of air masses associated with different moisture sources [Noone *et al.*, 2011] and more generally a wide variety of processes related to atmospheric convection and large-scale transport [Webster and Heymsfield, 2003; Galewsky *et al.*, 2011; Tremoy *et al.*, 2012]. Moreover, the isotopic composition of water vapor offers continuous and higher-frequency information compared to precipitation alone, and simultaneous measurements in both phases allow us to investigate exchange processes between water vapor and falling rain droplets [e.g., Lee *et al.*, 2006; Wen *et al.*, 2010].

To that aim, we have been recording simultaneous measurements of near-surface humidity and isotope ratios of both precipitation and water vapor in Niamey (Niger) since July 2010. These measurements over the first year (July 2010 to May 2011) showed a strong potential for investigating convective processes during rain systems and especially those affecting the moisture budget within cold pools [Tremoy *et al.*, 2012]. In this study, we investigate the relationship between the isotopic composition of both water vapor and rain and convective activity at the subrain event time scale through measurements from the 2010, 2011, and 2012 West African monsoon seasons.

Data and methods are described in section 2, whereas all the results are included in section 3. Concluding remarks are given in section 4.

2. Data and Methods

The isotopic composition of water ($\delta^{18}\text{O}$ and δD) is expressed in per mil through the δ notation given by

$$\delta = \left(\frac{R_{\text{sample}}}{R_{\text{VSMOW}}} - 1 \right) \times 1000$$

where R is the ratio between heavier (HD^{16}O or H_2^{18}O) molecules over lighter molecules (H_2^{16}O). R_{sample} is

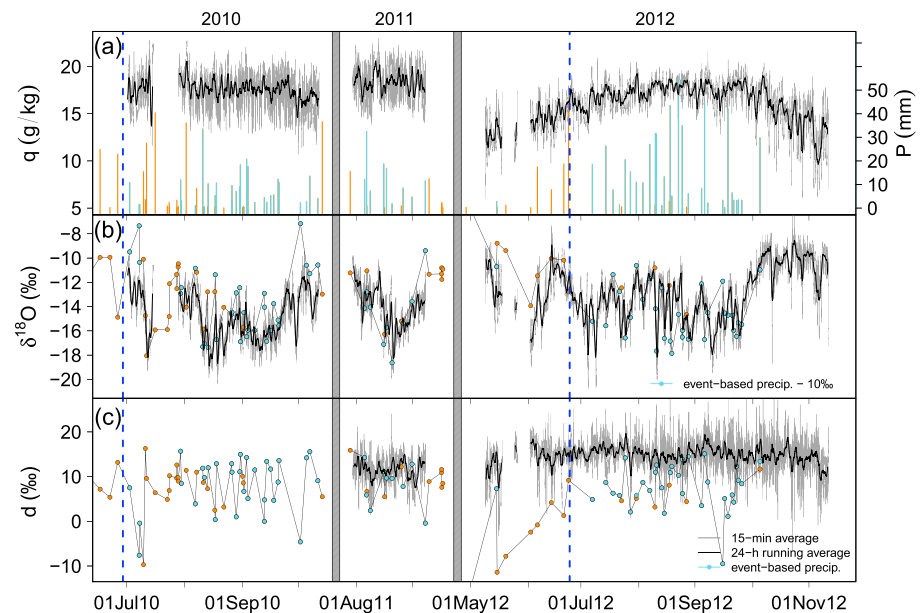


Figure 1. Data set recorded at IRI during the 2010, 2011, and 2012 monsoon periods: Time series of (a) specific humidity q (g/kg) along with event-based rainfall amount P (mm): light blue bars for selected events (see section 2.1) and orange bars for others and (b) $\delta^{18}\text{O}_v$ (‰): gray and dark lines are 15 min averages and 24 h running averages, respectively. Event-based ($\delta^{18}\text{O}_p - 10$) (‰) are in light blue dots for selected events and orange dots for others. (c) Same as Figure 1b but for deuterium excess. Water vapor deuterium excess is not available during the 2010 monsoon. Vertical dashed blue lines represent monsoon onset dates (29 June in 2010 and 22 June in 2012, see section 2.3).

the ratio of the measured sample (precipitation, atmospheric water vapor), whereas R_{VSMOW} is the ratio of reference (all data are given relative to the Vienna standard mean ocean water (VSMOW)). Thus, δ measures the enrichment or the depletion in heavier isotopologues relative to VSMOW. To first order, $\delta^{18}\text{O}$ and δD vary in proportion of about 8. The combination of $\delta^{18}\text{O}$ and δD leads to the second-order parameter d excess: $d = \delta\text{D} - 8 \times \delta^{18}\text{O}$ [Dansgaard, 1964], which reflects differences in HD^{16}O and H_2^{18}O behavior during nonequilibrium fractionation.

Figure 1 presents the data set recorded in Niamey during the 2010, 2011, and 2012 monsoon periods (June to October). Near-surface water vapor isotope ratios (see section 2.1 for details) are represented by gray and black lines for 15 min and daily time scales, respectively. Event-based measurements from a manual rain gauge (see section 2.2 for details) are represented by colored histograms and overplotted markers with lines for precipitation amounts and the isotopic composition of rain, respectively.

2.1. Water Vapor Measurements

Water vapor measurements have been recorded by a Picarro instrument (L1102-i model) which is based on Wavelength-Scanned Cavity Ring Down Spectroscopy. Specific humidity (q) and the isotopic composition of water vapor ($\delta^{18}\text{O}_v$ and δD_v) have been measured simultaneously in surface air in Niamey (Niger) at Institut des Radio-Isotopes (IRI, 13.5048°N, 2.0846°E, 218 m asl) since July 2010 [Tremoy et al., 2012]. Measurements started on 2 July 2010 and ran continuously until 13 October (the last rain event of the 2010 monsoon) except from 14 to 28 July when the analyzer malfunctioned. Unfortunately, power problems prevented us from recording data during the whole 2011 monsoon period. Data were only recorded during the core of the 2011 monsoon, from 29 July to 6 September. The whole 2012 monsoon period was recorded.

Our experimental setup is described by Tremoy et al. [2011]. In short, the instrument is installed in a temperature-regulated laboratory, around 20°C, with fluctuations on the order of 1°C over 24 h. Air is sampled continuously at 6 m above soil (1 m above roof) through a heated intake of 10 m, 3/8 inch diameter tubing. The sample line air is pumped at approximately 0.4 L/min. Unfortunately, the use of Synflex material as inlet during the 2010 monsoon period led to unsatisfactory precision on d_v . This material induces a longer response time in δD_v compared to $\delta^{18}\text{O}_v$ and leads to an erroneous signal in d_v [Schmidt et al., 2010].

Table 1. June Through October Sahelian Rainfall Indexes Relative to the 1900–2012 Period^a

Period	JJASO Sahel Index	All Rain Events at IRI		Selected Rain Events at IRI	
	Relative to 1900–2012 (mm/month)	Number	Accumulated P (mm)	Number	Accumulated P (mm)
1930–1969	+9.88	-	-	-	-
1970–2012	-11.56	-	-	-	-
2010	+16.06	64	524.3	31 (0)	242.1
2011	-10.01	41	354.6	9 (9)	113.7
2012	+8.81	49	615.5	34 (34)	512.0
Total		154	1494.4	74 (43)	867.8

^aNumber and accumulated precipitation of all rain events at IRI for 2010, 2011, and 2012 and for selected events during the same years for which both the isotopic composition of precipitation and water vapor have been measured at the same time. The number of events where water vapor deuterium excess (d_v) is available is indicated into brackets.

Therefore, the Synflex inlet was replaced with a perfluoroalkoxy (PFA) inlet in March 2011. We showed in laboratory experiments that the response time to obtain 99% of the change in d_v measurements using a 10 m PFA tubing line is shorter than 2 min for an instantaneous change in the vapor isotopic composition of -10‰ and $+5\text{‰}$ for $\delta^{18}\text{O}_v$ and d_v , respectively [Tremoy, 2012]. Since $\delta^{18}\text{O}_v$ variations during rain events in Niamey never exceed -10‰ and are on the order of $+8\text{‰}$ for d_v over periods much longer than 2 min (see section 3.2), we can discuss in this study d_v measurements of rain events for the 2011 and 2012 events.

As described by Tremoy et al. [2011], our data processing method consists of the following: first, averaging the data over a 5 min interval to reduce the signal-to-noise ratio (the frequency of data acquisition is about 6 to 10 s) and then, applying corrections to account for (1) humidity dependence and (2) isotopic calibration to VSMOW reference scale. Both corrections are determined using a home-made syringe pump system [Tremoy et al., 2011]. They are checked in the field over time to account for eventual drift. This system allows us to inject vaporized water standards continuously into the analyzer at different water vapor concentrations. The humidity dependence correction was checked 3 times (October 2010, March 2012, and August 2012), whereas the isotopic calibrations were performed on a daily to weekly time scale, using two water standards injected at a reference water vapor concentration of 20,000 ppm.

The syringe pump system also enables us to characterize the performances of the analyzer. The short-term precision of the instrument ($\pm 1\sigma$ during a 15 min stable measurement of a vaporized water standard) is better than $\pm 0.2\text{‰}$ and $\pm 0.8\text{‰}$ for $\delta^{18}\text{O}_v$ and δD_v , respectively, leading to a measurement precision better than $\pm 1.8\text{‰}$ for water vapor deuterium excess d_v .

2.2. Precipitation Measurements

During the 2010–2012 period, we collected 154 rain events with a manual rain gauge at IRI (cone-shaped SPIEA model 1650-02). During five events (2, 7, 11, 29 July 2010, and 15 September 2011), we also collected the rain at a higher frequency with a time step of 5 min. For each rain event, starting and ending times and precipitation rate at a 5 min time step were provided by an automatic rain gauge (T. Vischel, personal communication, 2012) located at IRI as part of the African Monsoon Multidisciplinary Analyses-Couplage de l'Atmosphère Tropicale et du Cycle Hydrologique observing system [Lebel et al., 2011]. The correlation coefficient (r) between manual and automatic precipitation amount from both IRI rain gauges is 0.98 (slope of 0.95, intercept of -0.21 mm) at the event scale over 2010–2012. The isotopic composition of the rain samples ($\delta^{18}\text{O}_p$ and δD_p) was analyzed by mass spectrometry. The accuracy and precision for $\delta^{18}\text{O}_p$ and δD_p are of $\pm 0.05\text{‰}$ and $\pm 0.5\text{‰}$, respectively (leading to an accuracy $\pm 0.7\text{‰}$ for deuterium excess, d_p).

The isotopic composition of water vapor was recorded for 74 of these 154 events by our laser instrument from 2 July 2010 to 1 October 2012 (see Table 1). We call them “selected events” hereafter. Table 2 lists relevant information about these events (starting and ending times, duration, precipitation amount). We will only discuss these events when we have simultaneously recorded the isotopic composition of both the atmospheric water vapor at a 5 min step and the precipitation during rain event.

Table 2. List of Rain Events Which Occurred in Niamey During the July to October 2010–2012 Period Where Both the Isotopic Composition of Water Vapor and Precipitation Phase Have Been Measured, Including Number of Events, Date and Starting Time, Duration, Accumulated Precipitation Recorded by the Manual Rain Gauge, Isotopic Classification Based on $\delta^{18}\text{O}_v$ Trend Along Each Event (See Text and Figure 6 for Details), and Possible Time Gap Between Significant Depletion of Water Vapor Before Beginning of Rainfall (Only for Classes A and B), With – (+) When Decrease in the Isotopic Composition of Water Vapor Precedes (Follows) Beginning of Rainfall^a

Number	Beginning Hour Date	Duration (min)	P (mm)	Class	Time Gap (min)
1	1415 UTC 2 Jul 2010	77	10.8	C+	
2	1650 UTC 7 Jul 2010	62	1.5	C+	+50
3	2235 UTC 7 Jul 2010	145	1.4	A+	–60
4	2045 UTC 29 Jul 2010	27	11.9	A'	–15
5	0540 UTC 30 Jul 2010	95	3.0	C+	
6	1810 UTC 6 Aug 2010	45	1.0	A+	
7	1525 UTC 10 Aug 2010	195	33.5	B'	
8	1235 UTC 11 Aug 2010	65	0.5	C+	
9	1315 UTC 13 Aug 2010	150	10.3	A+	
10	0755 UTC 17 Aug 2010	135	5.3	C+	
11	0015 UTC 18 Aug 2010	95	10.6	A+	–30
12	0400 UTC 26 Aug 2010	110	3.7	A+	–30
13	0805 UTC 26 Aug 2010	45	9.5	C+	
14	1405 UTC 28 Aug 2010	150	7.1	B'	
15	1045 UTC 30 Aug 2010	210	8.9	A'	
16	1905 UTC 30 Aug 2010	120	18.3	A+	
17	1710 UTC 1 Sep 2010	60	0.4	A+	
18	0345 UTC 3 Sep 2010	70	20.7	A+	–10
19	2005 UTC 3 Sep 2010	185	17.6	B+	
20	1225 UTC 7 Sep 2010	50	2.4	A+	
21	1605 UTC 12 Sep 2010	25	4.5	C+	
22	1710 UTC 12 Sep 2010	55	0.5	A+	
23	2250 UTC 13 Sep 2010	10	2.5	A+	–20
24	0055 UTC 16 Sep 2010	20	5.3	A+	–10
25	1630 UTC 17 Sep 2010	10	5.6	A+	
26	0035 UTC 20 Sep 2010	15	12.2	A+	–15
27	1035 UTC 20 Sep 2010	120	10.8	C+	
28	2230 UTC 1 Oct 2010	90	2.3	B+	–90
29	0500 UTC 5 Oct 2010	50	2.7	C+	
30	2225 UTC 6 Oct 2010	175	13.5	A'	–30
31	0630 UTC 11 Oct 2010	25	4.0	B+	–20
32	0535 UTC 5 Aug 2011	170	12.2	A'	–40
33	0715 UTC 6 Aug 2011	110	32.4	B'	–20
34	0635 UTC 8 Aug 2011	150	7.2	A'	–20
35	1125 UTC 15 Aug 2011	140	18.7	A+	
36	2345 UTC 16 Aug 2011	25	16.8	A'	–90
37	2245 UTC 19 Aug 2011	105	1.8	A'	–90
38	2045 UTC 25 Aug 2011	20	8.4	A+	+20
39	1605 UTC 30 Aug 2011	25	4.7	A+	–30
40	1750 UTC 6 Sep 2011	160	11.5	C+	
41	2145 UTC 13 May 2012	65	2.8	A'	
42	0200 UTC 4 Jul 2012	215	18.4	B+	
43	0655 UTC 11 Jul 2012	175	26.3	B+	–45
44	0110 UTC 15 Jul 2012	30	4.7	C+	
45	0905 UTC 15 Jul 2012	70	1.9	C+	
46	1450 UTC 18 Jul 2012	75	1.4	B+	
47	1655 UTC 21 Jul 2012	55	20.5	A+	
48	0955 UTC 24 Jul 2012	260	15.3	B+	–20
49	1520 UTC 27 Jul 2012	60	11.0	A'	–20
50	0225 UTC 31 Jul 2012	185	10.7	A'	–60
51	1910 UTC 3 Aug 2012	215	27.0	B+	
52	1700 UTC 6 Aug 2012	85	29.1	A+	
53	2335 UTC 6 Aug 2012	90	1.9	C+	
54	0725 UTC 7 Aug 2012	295	31.4	A*	
55	0550 UTC 10 Aug 2012	95	1.1	B+	

Table 2. (continued)

Number	Beginning Hour Date	Duration (min)	P (mm)	Class	Time Gap (min)
56	1150 UTC 11 Aug 2012	315	13.2	A+	
57	1640 UTC 14 Aug 2012	225	43.5	B+	
58	1550 UTC 15 Aug 2012	15	5.1	B+	
59	0205 UTC 19 Aug 2012	330	55.7	B*	
60	0450 UTC 21 Aug 2012	105	34.9	A+	-15
61	0755 UTC 21 Aug 2012	105	0.3	C+	
62	1045 UTC 24 Aug 2012	30	6.1	A+	-15
63	1335 UTC 31 Aug 2012	25	8.3	B+	+20
64	0240 UTC 2 Sep 2012	115	44.5	B+	-10
65	2120 UTC 3 Sep 2012	10	2.1	A+	-10
66	2125 UTC 11 Sep 2012	15	3.3	A'	-20
67	2145 UTC 12 Sep 2012	65	0.3	B+	+30
68	1605 UTC 14 Sep 2012	25	41.9	B+	
69	1900 UTC 16 Sep 2012	390	6.4	A'	-30
70	1755 UTC 17 Sep 2012	25	3.3	B+	-15
71	0535 UTC 19 Sep 2012	180	3.2	B+	-30
72	0430 UTC 20 Sep 2012	60	3.5	A*	
73	0055 UTC 2 Sep 2012	110	3.3	A'	-10
74	1750 UTC 1 Oct 2012	205	29.8	C+	

^aNote that the isotopic classes include subclassifications: * stands for events where water vapor depletion is progressive during rain stage, instead of sharp; ' stands for events for which fluctuations occur during rain stage; and + (different from positive gap symbol) stands for all other events (see section 3.2.1).

2.3. Meteorological and Satellite Data

Classical meteorological variables are recorded at 2 m height at IRI with a time resolution of 10 min. For the 2010 and 2011 monsoon periods, we used a Thermo-Recorder TR-73U (T&D Corporation, Nagano, Japan) as presented in Tremoy *et al.* [2011]. This sensor measures the atmospheric temperature, relative humidity (RH), and barometric pressure with an accuracy of $\pm 0.3^\circ\text{C}$, $\pm 5\%$, and ± 1.5 hPa, respectively (at 25°C and for RH = 50%). We replaced this sensor in September 2011 with a Hobo Pro V2 (U23-001) data logger which measured temperature and relative humidity during the 2012 monsoon period. The accuracy of this data logger is $\pm 0.2^\circ\text{C}$ and $\pm 2.5\%$ for air temperature and humidity, respectively.

We used outgoing longwave radiation (OLR) gridded data set from the National Oceanic and Atmospheric Administration polar-orbiting satellites [Liebmann and Smith, 1996] in order to calculate the monsoon onset dates. Based on Fontaine and Louvet [2006] study, we averaged OLR data between two domains (10°W – 10°E , 0°N – 7.5°N) and (10°W – 10°E , 7.5°N – 15°N), and we calculated an OLR index by taking the temporal difference between the northern and southern regions. Then, the monsoon onset is detected when the lower frequency (10 day running mean) of this index becomes negative (on 29 June 2010, 13 June 2011, and 22 June 2012, see Figure 1).

In order to study the basic characteristics of each rain system, we used satellite precipitation estimates (3-hourly rain rate at $0.25^\circ \times 0.25^\circ$ resolution) from Tropical Rainfall Measuring Mission (TRMM 3B42) [Huffman *et al.*, 2007].

We also used radio-sounding TEMP data from fixed land stations (available at <http://weather.uwyo.edu/upperair/sounding.html>) from Niamey airport (13.48°N , 2.70°E). For this period, two launches per day were available, the first one at 00:00 UTC and the other one at 12:00 UTC.

2.4. Simple Box Modeling

We used a basic conceptual model based on water budget analysis to discuss the water isotopic response to MCS in Niamey. A description of the processes involved and their representation in the model is detailed below.

2.4.1. Processes Involved

The isotopic composition of water (vapor, condensate, and precipitation) in a MCS is sensitive to the phase changes and moisture transports which occur in the different parts of the system. Its temporal and spatial variability is controlled in part by the condensation height, the strength of mesoscale subsidence, the

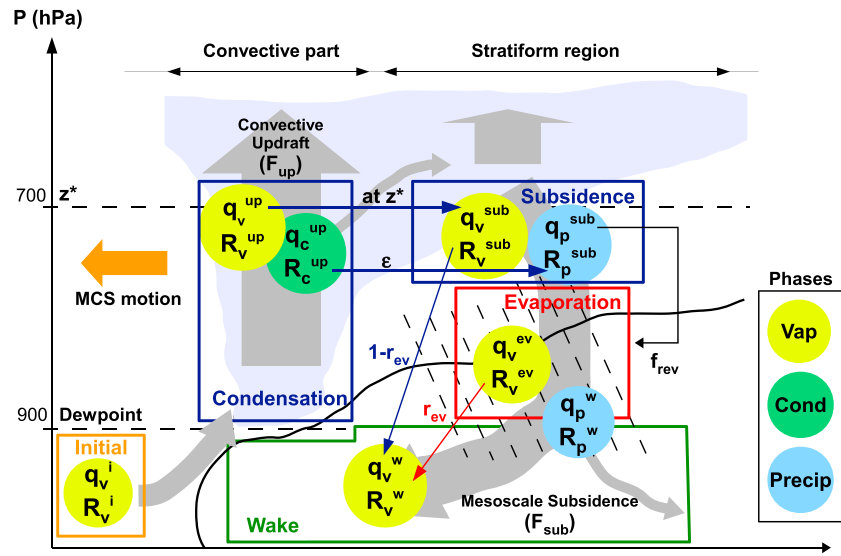


Figure 2. Schematic representation of the simple model applied to a MCS, where specific humidity q and isotope ratios R of condensate, vapor, and precipitation (subscript “c,” “v,” and “p,” respectively) are calculated in the different boxes. The initial air mass (superscript “i”) is dehydrated in the convective column (superscript “up”) through condensation, depleting the water vapor with increasing altitude z^* . Condensate and water vapor at z^* are then transferred to the subsidence box (superscript “sub”) where all condensate is converted to precipitation. In the stratiform region, a dry airflow enters the system at the rear toward the base of the convective part. Precipitation partially reevaporates and cools the subcloud region. Cold pool (wake box, superscript “w”) is fed both by the depleted air advected by mesoscale subsidence and admixture of moisture from rain evaporation (superscript “ev”) in unsaturated downdrafts. The resulting water vapor in the cold pool can also partially reequilibrates with the surrounding raindrops.

proportion of rain which is reevaporated, the diffusive exchanges between falling rain and water vapor, the entrainment of environmental air, and the surface evaporation.

Risi *et al.* [2010] suggested that the isotopic composition of precipitation along squall lines is mainly controlled by mesoscale subsidence of isotopically depleted air in unsaturated downdraft and admixture of isotopically enriched vapor from reevaporation of falling rain. Based on these results, we present here a conceptual simple model. The objective is to determine the relative contribution of mesoscale subsidence and rain evaporation to the isotopic composition of surface water vapor throughout rain events. Our model will thus focus on these two processes, not accounting for the others, as we would like to test the Risi *et al.* [2010] hypothesis.

Our model is based on the assumption that the isotopic composition of near-surface water vapor is only controlled by the advection of moisture from higher levels (mesoscale subsidence) and by rain evaporation processes. We present a box model that simulates the isotopic fractionation associated with the condensation of vapor in the convective column and the rain reevaporation in the stratiform part through mesoscale subsidence (Figure 2). The model contains four different boxes (condensation, subsidence, rain evaporation, and wake). Each of them represents a component of the convective system where a single process occurs and contributes to the final isotopic composition of water vapor in the cold pool (wake box). The objective is to describe the evolution of the isotopic composition of water vapor at the surface as a function of the relative contribution of these processes involved in the moisture budget. We detail below the four boxes.

2.4.2. Condensation Box

First, we simulate the isotopic composition of in-cloud water vapor and liquid condensate during the convective ascent (see Figure 2 and its legend). Mass conservation in the condensation box gives the following equation:

$$dq_v + dq_c + dq_p = 0 \tag{1}$$

where q_v is the water vapor mixing ratio, q_c is the mixing ratio of condensate, and q_p is the mixing ratio of precipitation.

Assuming that only vapor and cloud droplets coexist in the condensation box (no ice particle) and that the condensate forming the precipitation is at equilibrium with the water vapor and does not reevaporate in this box, the vertical evolution of the isotopic ratio of the vapor phase can be expressed following *Merlivat and Jouzel [1979]*:

$$\frac{dR_v}{R_v(z)} = \frac{(\alpha - 1) \cdot dq_{vs} - q_c \cdot d\alpha}{q_{vs}(z) + \alpha(z) \cdot q_c} \quad (2)$$

where α is the equilibrium fractionation coefficient for liquid-vapor which only depends on temperature and should also take into account kinetic fractionation during solid condensation for negative temperature, but we neglect it in this model. At saturation q_{vs} is the specific humidity q_v . The fraction of condensate which is converted to precipitation during the condensation is usually defined as the precipitation efficiency ε ($0 < \varepsilon < 1$):

$$\varepsilon = -\frac{dq_p}{dq_v} \quad (3)$$

Using equations (1) and (3), the mixing ratio of condensate q_c can be expressed as

$$q_c = (1 - \varepsilon) \cdot (q_v^i - q_v(z)) \quad (4)$$

where superscript i stands for initial.

In the case where $\varepsilon = 1$, all the condensate is immediately removed from the system and the condensation process follows a classical Rayleigh distillation. In the case where $\varepsilon = 0$, no precipitation falls out the condensation box; the system is closed.

Considering an air mass with an initial thermodynamic state corresponding to observations (temperature, specific and relative humidity, dew point), we define a linear vertical gradient of temperature and corresponding q_{vs} , based on radio-sounding measurements in Niamey before the arrival of the MCS (see Figures 3a and 3b). We thus calculate the vertical gradient of the fractionation coefficient α as it depends on temperature. Equation (2) is numerically solved with a simple iterative method, from the lifting condensation level (LCL, estimated from surface measurements) to an altitude z^* . At the LCL, we initialize the water vapor isotope ratio using the mean isotopic composition during initial stage of the considered event and of the condensate (R_c) which is assumed to form in equilibrium with the vapor at all level (Figures 3c and 3d).

2.4.3. Subsidence Box

We define z^* as the level where air masses depleted by previous condensation are transferred to the subsidence box, before being advected downward in the stratiform part (Figure 2). Taking $z^* \leq 5$ km (~ 550 hPa) represents a reasonable approximation for this level in the stratiform part [*Houze, 2004*] (see section 3.3 for sensitivity tests on z^*).

Water transport from convective to stratiform zone mainly occurs above z^* altitude [*Chong and Hauser, 1990; Caniaux et al., 1994*]. We assume that specific humidity, condensate content, and isotope ratios entering the subsidence box are taken at z^* in the condensation box (Figure 3c). This hypothesis may underestimate q_v^{sub} and δ_v^{sub} when the entrainment of environmental air below z^* is important. q_v^{sub} , R_v^{sub} , and R_p^{sub} (see Figure 2 caption) are then transported downward by mesoscale subsidence. They constitute the initial composition of the vapor and precipitation into the unsaturated downdraft where evaporation of falling rain occurs.

It is worth noting that no isotopic fractionation occurs in this box, which can be considered actually as a transfer box.

2.4.4. Evaporation Box

In the evaporation box, the isotopic fractionation associated with droplet reevaporation and diffusive exchanges between vapor and rain are based on the theory developed by *Stewart [1975]* (also well described in *Bony et al. [2008]*). Physically, it depends on the relative humidity h in the unsaturated downdraft. The reevaporated fraction of an average droplet f_{rev} is all the more important when relative humidity is low. We make the simplification that the evaporation box is homogeneous along a vertical profile.

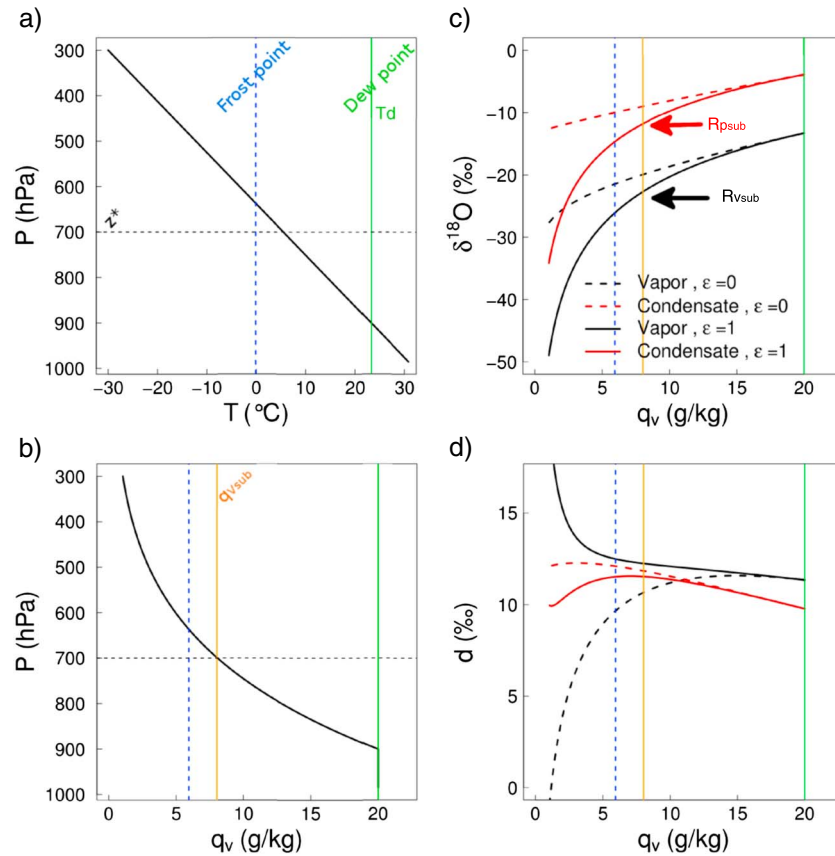


Figure 3. This is an example based on the 15 August 2011 event (initial state: temperature of 30.8°C, specific humidity $q_v^i = 17.9$ g/kg, relative humidity of 62.4%, and dew point of 23.3°C). LCL is at 1500 m (~985 hPa) and final z^* at 775 hPa, and the isotope ratio at this level is $\delta^{18}O_v^i = -13.3\text{‰}$ and $d_v^i = 11.3\text{‰}$. Vertical profiles of (a) temperature T and (b) specific humidity q_v ($q_v = q_{vs}$ for $T < T_d$) defined along the condensation box, of (c) $\delta^{18}O$ and (d) d – excess versus q_v , along the condensation process. Black lines are for vapor, whereas red lines are for liquid condensate which is assumed to be in equilibrium with the vapor. Solid and dashed lines correspond to a Rayleigh distillation ($\epsilon = 1$) and a closed system ($\epsilon = 0$), respectively. In-cloud reevaporation of the condensate is neglected in the model. Frost point is represented by the blue dashed line and dew point by the green solid line. The intersection between $q_v(z^*) = q_v^{sub}$ (orange solid line) and $\delta^{18}O$ of vapor or condensate in Figure 2c gives the isotope ratios in the subsidence box (R_p^{sub} and R_v^{sub}).

Figure 4 illustrates the behavior of the isotopic composition of vapor and raindrop as a function of f_{rev} . We observe that evaporation tends to enrich the isotopic composition of water vapor and that deuterium excess in water vapor is higher after the evaporation process. It is important to underline that for certain cases, the combination of low f_{rev} and low relative humidity leads to a decrease in the isotopic composition of vapor. Moreover, the isotopic composition of precipitation and water vapor is not linearly dependent on f_{rev} and water vapor deuterium excess can sharply increase for low f_{rev} and then progressively decreases with raindrops getting more and more reevaporated.

It is worth noting that when the relative humidity tends toward 1 (air is closed to saturation), reevaporation cannot occur (f_{rev} tends toward 0), and diffusive exchanges take place between the droplets and the surrounding vapor. This enables the precipitation to reequilibrate with the surrounding vapor. On the other hand, when h tends toward 0, precipitation cannot reequilibrate with the vapor, and the rain evaporation process dominates [see also *Bony et al., 2008*].

2.4.5. Wake Box

Water vapor in the wake box results from the combination of water vapor from subsidence and evaporation processes as defined in the corresponding boxes (see Figure 2 and sections 2.4.3 and 2.4.4). The isotopic composition of water vapor in this box will be compared to our observations. For the sake of simplicity, we

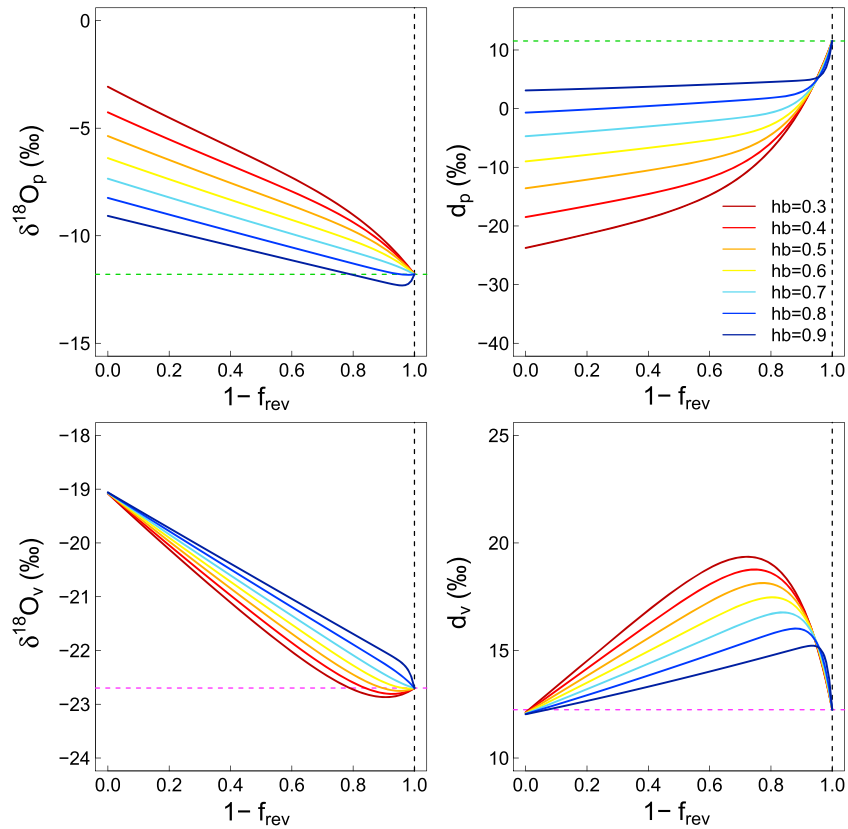


Figure 4. Evolution, in the evaporation box, of the isotopic composition of water vapor and precipitation as a function of the fraction f_{rev} of an average droplet that is reevaporated. Initial conditions are $\delta^{18}O_v^i = -22.7\text{‰}$, $\delta^{18}O_p^i = -11.8\text{‰}$, $d_v^i = 12.2\text{‰}$, and $d_p^i = 11.5\text{‰}$. They correspond to the outputs of condensation box at $z^* = 775$ hPa (subsidence box) for the 15 August 2011 event. The ratio M [see Bony *et al.*, 2008] between initial vapor and rain masses is taken at 2 in this example. Sensitivity to the relative humidity (h_b) in the unsaturated downdraft is shown by the different color lines.

assume that the wake box is vertically homogeneous. Mass conservation for humidity and water vapor isotopic ratio gives

$$q_v^w = q_v^{ev} + q_v^{sub} \tag{5}$$

$$R_v^w = r_{ev} \cdot R_v^{ev} + (1 - r_{ev}) \cdot R_v^{sub} \tag{6}$$

where r_{ev} is the percentage of water vapor in the wake box arising from the reevaporation of rain:

$$r_{ev} = \frac{q_v^{ev}}{q_v^{ev} + q_v^{sub}} \tag{7}$$

An estimate of f_{rev} is deduced from q_v^{ev} (moisture arising from rain evaporation) and thus from r_{ev} . Indeed, this parameter is needed in the isotopic calculation at evaporation and accounts for the liquid/vapor ratio, named $M = q_{v0}/q_{p0}$ (see Bony *et al.* [2008] and Appendix A).

2.4.6. Main Model Characteristics

We describe below the main successive steps of the model, introducing the temporal evolution of each parameter and thus the evolution of the isotopic composition of both water vapor and rain:

1. First, we define an arbitrary temporal evolution of z^* . At the initial stage, z^* is taken at LCL level (~985 hPa). Then z^* increases from $t = t_0$, corresponding to the arrival of the gust front, to the rear of the system in the subsidence region ($z^* \leq 700$ hPa, sensitivity to z^* is discussed in section 3.3).
2. Then, the vertical profiles of the isotopic composition are calculated into the condensation box, depending on the vertical profiles of temperature and humidity which are forced in the box. In the following, we set $\epsilon = 1$ for simplicity (all the condensate is removed). However, we briefly discuss the sensitivity on ϵ in section 3.3.

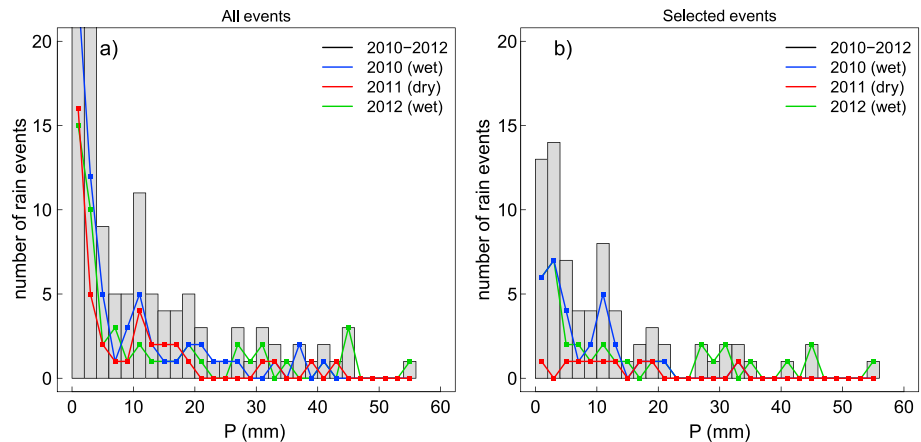


Figure 5. (a) Distribution of precipitation amounts at IRI for all rainfall events during 2010–2012 (gray histogram), 2010 (blue points and line), 2011 (red points and line), and 2012 (green points and line). (b) Same as Figure 5a but only for the 74 selected rain events reported in Table 2.

3. Both water vapor mixing ratio and isotopic composition at z^* are transferred to the subsidence box without fractionation. If z^* does not vary with time, then q_v^{sub} and R_v^{sub} are constant.
4. We calculate q_v^{ev} from the difference between specific humidity measurement q_v^{meas} and q_v^{sub} estimation (equation (5)) and then r_{ev} from equation (7).
5. We calculate the temporal evolution of f_{rev} and M using equations (A4) and (A6) as defined in Appendix A.
6. We calculate R_v^{ev} , using the equations of Stewart [1975] and Bony *et al.* [2008], relative humidity measurements, and the estimate of f_{rev} .
7. Finally, we calculate the isotopic composition of water vapor (of the wake box) resulting from both processes as a function of time, using equation (6). The final isotopic composition of precipitation corresponds to the one calculated in the evaporation box.

3. Results

3.1. Rainfall Events Features

At the regional scale, the Sahel rainfall index (the June through October precipitation anomalies with respect to 1900–2012 and averaged over 10°N – 20°N and 20°W – 10°E [Janowiak, 1988, available at <http://jisao.washington.edu/data/sahel/>]) reveals that the 2010, 2011, and 2012 monsoons over West Africa (June to October) have contrasting rainfall characteristics (see Table 1). The wettest year is 2010 and 2012 is the fourth wettest year since 1970 and the severe drought that started in the Sahel. On the contrary, 2011 is more representative of the drought period. Indeed, the June through October precipitation average over (10°N – 20°N , 20°W – 10°E) is +16.06, –10.01, and +8.81 cm/month relative to the 1900–2012 period in 2010, 2011, and 2012, respectively.

Interestingly, although there were 15 fewer rain events in 2012 compared to 2010, the 2012 monsoon was wetter at the local scale (the annual precipitation amount at IRI was 524.3, 354.6, and 619.5 mm in 2010, 2011, and 2012, respectively, Table 1).

Figure 5a presents the distribution of the amount of precipitation for the 154 rain events collected between 2010 and 2012. Seventy rainfall events have a precipitation amount lower than 5 mm (46% of all events). The other 84 events explain 91% of the total precipitation amount over the 3 years (1494.4 mm). The distribution of precipitation amount for the 74 selected events is quite consistent with that of all events, despite a smaller number of extreme weak rainfall events (see Figure 5b). Forty-one percent of the selected rainfall events (30 events) have precipitation amount lower than 5 mm, and the other half explain 92% of the total precipitation (867.8 mm).

The mean duration of selected events is 107 ± 84 min (ranging from 10 to 390 min), suggesting that we recorded different types of rain events, from local convective events to well-organized long-lived MCS (Table 2).

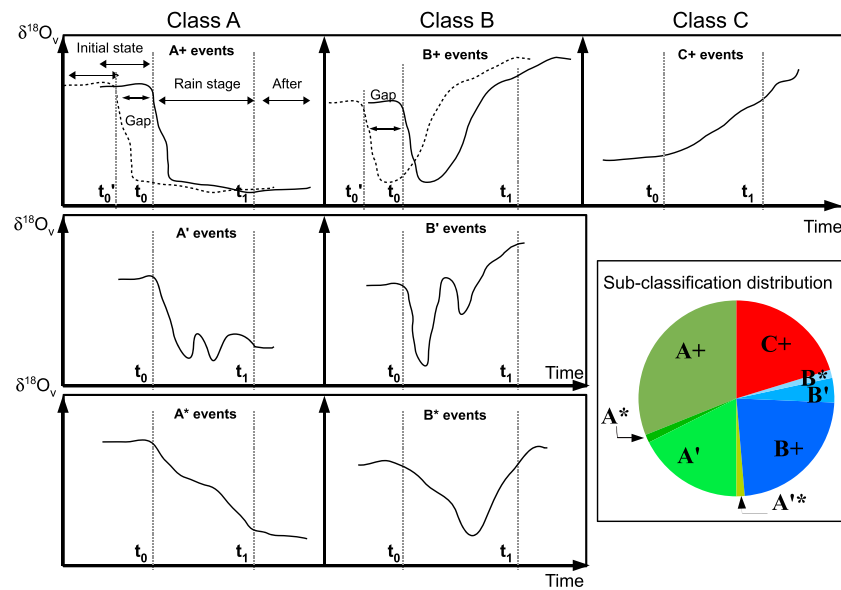


Figure 6. Idealistic representation of the three isotopic classes (A, B, and C) based on $\delta^{18}\text{O}_v$ temporal evolution along rain systems at IRI. The initial stage is defined as the 30 min interval preceding the rain start (t_0). Rain stage spans from t_0 to the end of rain t_1 , and the after rain stage corresponds to the 30 min interval succeeding t_1 . Classes A and B generally record a drop in $\delta^{18}\text{O}_v$ in phase with temperature drop associated with raindrops evaporation; these drops do not necessarily occur at the beginning of rain but may sometimes happen with some delay before rain start (at t_0 , dashed line). Contrary to class A, class B events show an increasing trend in $\delta^{18}\text{O}_v$ during rain stage. Events A and B showing a progressive isotopic decrease are denoted by asterisk. This asterisk classification reflects that the isotopic drop at the initial stage remains longer than the temperature one. Events A and B where strong δ fluctuations occurred during rain stage are denoted by prime (see Table 2). $\delta^{18}\text{O}_v$ from class C events also increases during rain stage but do not record a drop at t_0 . Both classes A and B include cross-, prime-, and asterisk-type events, whereas class C only includes cross-type events. The distribution of all subclassifications is also represented by the pie chart. Classes A, B, and C account for about 51.35%, 28.38%, and 20.27% of the 74 selected rain events, respectively.

3.2. Robust Isotopic Features

3.2.1. Water Vapor Isotopic Classification

Among the 74 selected rain events, we observe several types of evolution regarding the isotopic composition of water vapor. A first step consists of classifying these different events, based on the evolution of $\delta^{18}\text{O}_v$ at different temporal stages: the initial stage is defined as the 30 min period before the rain starts or before the decrease in surface temperature when it occurs with a delay with respect to the rain start. Indeed, the arrival of convective systems is associated with a decrease in surface temperature, due to the propagation of cold pool initiated by the evaporation of falling precipitation in unsaturated downdrafts [Zipser, 1977; Caniaux *et al.*, 1994]. The second stage corresponds to the rain period, and the after rain stage corresponds to the 30 min period after the end of rainfall.

We defined three different classes (see Figure 6). The first category (class A) corresponds to events where $\delta^{18}\text{O}_v$ decreases in phase with the decrease in air temperature and stays relatively constant during the rain below the initial value. Class B corresponds to events for which we also observe a decrease of $\delta^{18}\text{O}_v$ with temperature at the beginning, but then, $\delta^{18}\text{O}_v$ increases significantly during the rainfall, and the final value is higher than (or close to) the initial value. For these two classes, the decrease in $\delta^{18}\text{O}_v$ and temperature may sometimes occur before the rain start. This is in agreement with the fact that cold pools propagate around the convective system and thus can be detected even in the absence of rain. For those cases, the observed possible time gap between changes in $\delta^{18}\text{O}_v$ and the onset of rain is indicated in Table 2. For both classes, we also distinguished events where depletion at the beginning is sharp or more progressive, reflecting that the drop at the initial stage lasts longer for isotopes than for temperature (2 and 1 events for classes A and B, respectively, in this latter case, denoted by * in Table 2 and represented in Figure 6), and events where strong fluctuations occurred during the rain stage (14 and 3 events for classes A and B, respectively,

Table 3. Statistics for Each Class and Subclassification: Number of Events Represented by Each Class, Percentage of the Number of Events, and Total Precipitation for the 74 Selected Events Reported in Table 2^a

Class	Subclass	Number of Selected Events	Percentage of Selected Events	Percentage of Total Precipitation	Mean Duration of Rainfall (min) $\pm 1\sigma$
A	A+	23 (9)	31.08	26.79	76 \pm 70
	A'	13 (10)	17.57	12.64	130 \pm 102
	A*	1 (1)	1.35	3.62	295 \pm 0
	A**	1 (1)	1.35	0.40	60 \pm 0
	Total	38 (21)	51.35	43.45	100 \pm 90
B	B+	17 (14)	22.97	30.35	118 \pm 84
	B'	3 (1)	4.05	8.41	152 \pm 43
	B*	1 (1)	1.35	6.42	330 \pm 0
	Total	21 (16)	28.38	45.18	133 \pm 90
C	C+	15 (6)	20.27	11.37	89 \pm 50
	C'	0 (0)	-	-	-
	C*	0 (0)	-	-	-
	Total	15 (6)	20.27	11.37	89 \pm 50

^aNote that +, ', and * subclassifications are included in the total of each class. The number of events where water vapor deuterium excess (d_v) is available is indicated into brackets.

in this case, denoted by ' in Table 2 and represented in Figure 6). For both classes, the events which are not included in ' and * subclassifications are denoted by + (see Figure 6 and Table 3). The sharp decreases in $\delta^{18}\text{O}_v$ between the initial and the rain stage ranges from -1.1‰ to -4.5‰ ($m = -2.5 \pm 1.1\text{‰}$) considering class A events (A* discarded) and from -0.6‰ to 5.0‰ ($m = 2.7 \pm 1.5\text{‰}$) considering class B events (B* discarded). Class C is associated with increasing in $\delta^{18}\text{O}_v$ from the beginning to the end of the rainfall, and no sharp depletion is seen between the initial stage and the rain stage. Class A accounts for 51.35% of the selected rain events and explains 43.32% of the total precipitation, whereas class B and class C account for 28.38% and 20.27%, respectively, and explain 45.24% and 11.43% of the total precipitation, respectively (see Table 3).

This qualitative classification is only based on the general behavior of $\delta^{18}\text{O}_v$ with time (we do not use d_v behavior here). Figure 7 shows examples of the temporal evolution of temperature, humidity, and the isotopic composition of water vapor during rainfall events which are representative of these three categories. We observe that humidity measurements may sometimes have a different behavior than $\delta^{18}\text{O}_v$ during the rain stage. For example, on 15 August 2011, specific humidity strongly decreases, from 19 to 16 g/kg along with $\delta^{18}\text{O}_v$ at the beginning of the event, but it increases over the second half of the event (Figure 7). This demonstrates that the isotopic composition of water vapor brings additional information regarding the control of humidity at the surface during rainfall.

Moreover, we observe a robust and sharp increase in d_v in phase with $\delta^{18}\text{O}_v$ and temperature drop at the transition between the initial stage and the rain stage for classes A and B. This sharp increase ranges from $+4.0\text{‰}$ to $+16.0\text{‰}$ ($m = 8.8 \pm 3.6\text{‰}$) considering class A events and from $+2.4\text{‰}$ to $+16.2\text{‰}$ ($m = 8.6 \pm 4.3\text{‰}$) considering class B events (Figure 7). This feature is not a measurement artifact due to a tubing line memory effect (see section 2.1). The sharp increase in d_v is then followed by a progressive decrease as rain falls, which is usually more pronounced for class B events. On the contrary, class C events do not systematically record any significant sharp increase in d_v at the initial rain stage transition and/or significant decreasing trend during rainfall.

3.2.2. Temporal Evolution of δ and Meteorological Parameters for Each Class

For each class, we performed statistical analyses on the isotopic composition of water vapor and on meteorological parameters as a function of the temporal stages of the rain event. To that aim, we averaged the different parameters over the three stages as defined in section 3.2.1, after having removed the daily mean to each value. To illustrate the temporal evolution of these parameters, we show their distributions for each class on box plot diagrams (lower extreme values, extreme of the lower whisker, lower quartile, median, upper quartile, extreme of the upper whisker, upper extreme values), using a definition of 1.5 times the interquartile range for the whisker. The distributions are represented as the difference from the initial stage for each class.

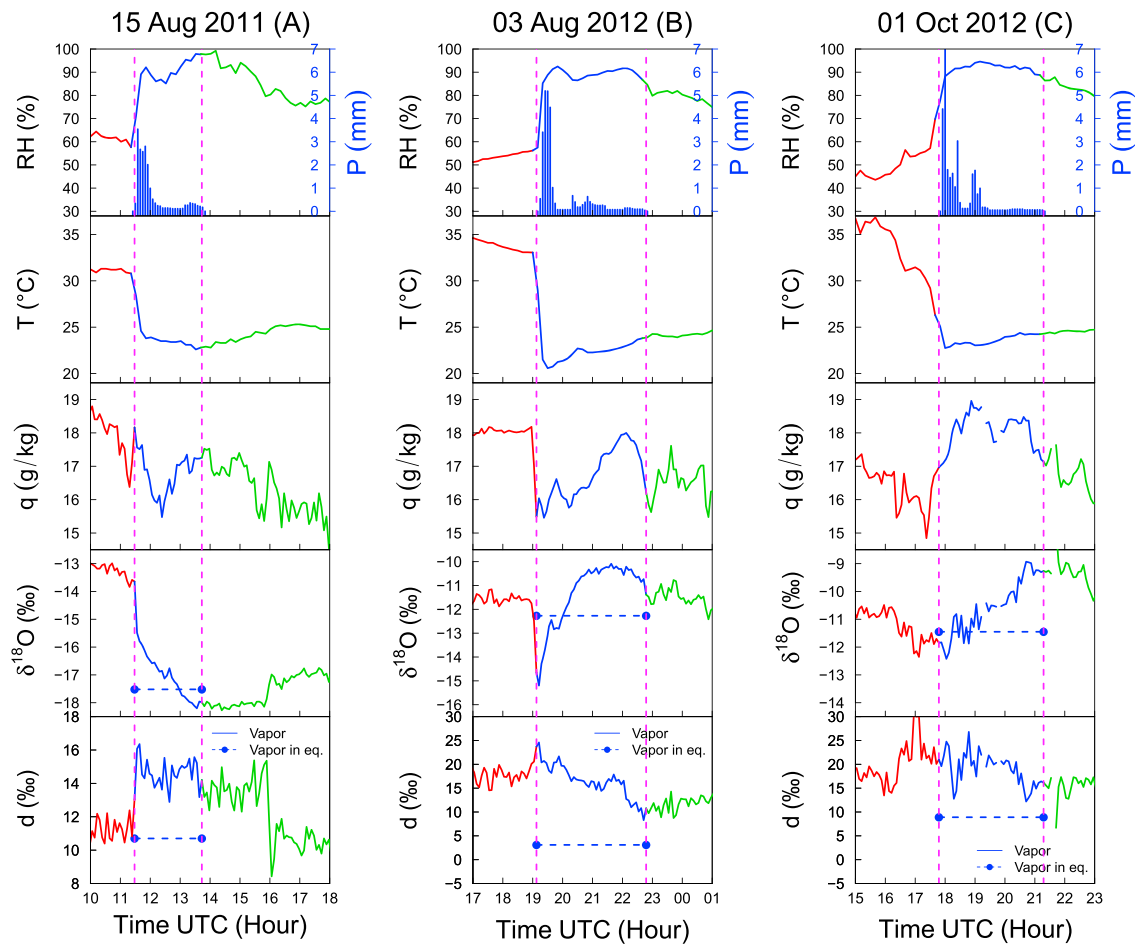


Figure 7. Three examples of events corresponding to the three isotopic classes (A: left column, B: middle column, and C: right column) as defined in section 3.2: temporal evolution at a 5 min resolution of surface relative humidity (in %) along with precipitation amount (right blue axis, in mm), air temperature (in °C), specific humidity q (in g/kg), and $\delta^{18}\text{O}$ and d of water vapor (solid and colored line, in ‰). Pink dotted lines are limits between initial, rain, and after rain stages. Mean $\delta^{18}\text{O}$ and d theoretically in equilibrium with the water vapor (horizontal blue dashed line) are calculated from precipitation mean composition averaged over the rainfall period (see section 3.2.4).

Figure 8 shows the box plot diagrams for q , $\delta^{18}\text{O}_v$, and d_v measurements during the three stages, considering all selected events. These diagrams illustrate the isotopic classification we have described above and the different effects that rain events may have on the isotopic composition of cold pools water vapor. We clearly observe the three different types of $\delta^{18}\text{O}_v$ evolution. On average, class A events exhibit a decrease in q and $\delta^{18}\text{O}_v$ by -0.7 ± 1.1 g/kg and -1.9 ± 1.3 ‰, respectively, whereas class C events tend to have an increase in q and $\delta^{18}\text{O}_v$ by $+1.0 \pm 0.6$ g/kg and $+0.8 \pm 0.9$ ‰, respectively. Differences between the rain stage and the initial stage for class B events are -0.4 ± 1.0 g/kg and -1.2 ± 1.0 ‰ for q and $\delta^{18}\text{O}_v$, respectively. Class B is actually an intermediate between classes A and C, as it includes rain events where depletion dominates at the beginning (as in class A) and where enrichment dominates at the end of the event (as in class C). During rain stage, d_v increases by 2.3 ± 2.1 ‰, 1.1 ± 2.1 ‰, and 0.5 ± 1.5 ‰ for classes A, B, and C, respectively. This may reflect the role rain evaporation plays in the control of the isotopic composition of water vapor as deuterium excess is very sensitive to this process (see section 2.4.4).

Regarding the temperature evolution, Figure 9a indicates that class B events record the strongest cooling of surface air ($-5.2 \pm 1.8^\circ\text{C}$), whereas temperature drops are weaker for class C ($-2.2 \pm 2.2^\circ\text{C}$), and intermediate for class A ($-4.3 \pm 2.0^\circ\text{C}$). This suggests that class B events are mostly associated with more intense cold pools. This temperature feature is consistent with the temporal evolutions of relative humidity which show larger increases for class B ($+16.5 \pm 8.9\%$) than for class A ($+13.4 \pm 10.7\%$) and for

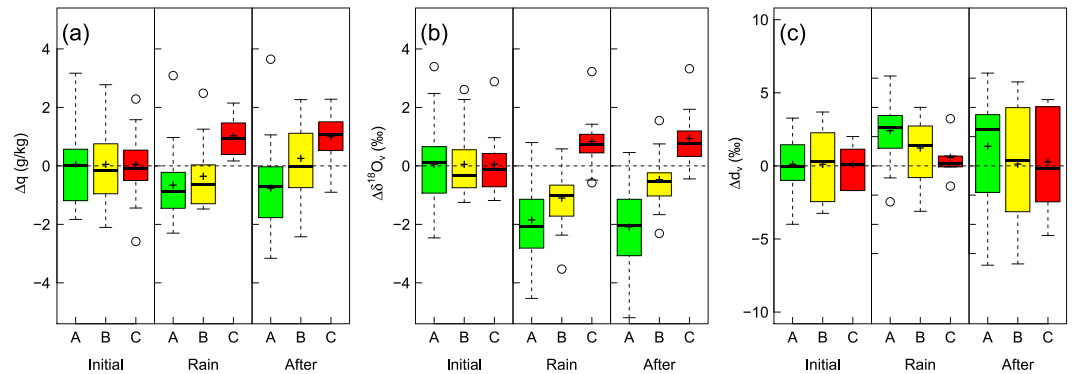


Figure 8. Statistical values (lower and upper quartile, median, spread, and mean represented by black crosses) of temporal changes in surface (a) q (g/kg), (b) $\delta^{18}O_v$ (‰), and (c) d_v (‰) relative to the mean distribution during the initial stage for each of the three classes (A, in green; B, in yellow; and C, in red) as defined in section 3.2.

class C ($+11.0 \pm 10.8\%$) during the rain stage compared with the initial stage (Figure 9b). Moreover, relative humidity during the different stages shows different distributions for each class (Figure 9c). We observe that relative humidity is generally higher for class B events than for classes A and C. For example, during the rain stage, the median (lower quartile) is 78.4% (70.6%), 85.0% (76.5%), and 77.5% (65.8%) for classes A, B, and C, respectively.

3.2.3. Characteristics of Precipitation Versus Isotopic Classification

For each class, we computed the mean duration of rain events (Table 3). The distribution of rain events duration (see Figure 10a) show that class B includes longer rain events than class C. We also calculate for each class the average precipitation rate from TRMM data during each selected rain event over the $10^\circ W$ – $10^\circ E$ and $0^\circ N$ – $20^\circ N$ domains (Figure 11a). These composite maps clearly show that classes A and B rain events correspond to more organized and intense convective systems than class C. This feature is even more obvious when looking at the median of TRMM precipitation rate (Figure 11b). Indeed, precipitation rates averaged over a $3^\circ \times 3^\circ$ resolution box and centered onto the Niamey coordinates are 1.4 mm/h, 1.5 mm/h, and 0.5 mm/h for classes A, B, and C, respectively. Locally, the mean precipitation rate in Niamey grid point is quite similar for class A (2.3 ± 4.1 mm/h) and for class B (2.8 ± 4.3 mm/h) and weaker for class C (1.2 ± 1.8 mm/h). These values are in agreement with the precipitation rates recorded by the rain gauge at IRI, which are on average of 11.0 ± 11.7 mm/h, 12.8 ± 21.3 mm/h, and 4.8 ± 4.1 mm/h for classes A, B, and C, respectively, although class B exhibits higher precipitation amounts (see the precipitation amount distributions at IRI in Figure 12a). The local distribution of number of rain events as a function of precipitation amount ranges for each class (Figure 10b) confirms that classes A and B correspond to more intense rainfalls.

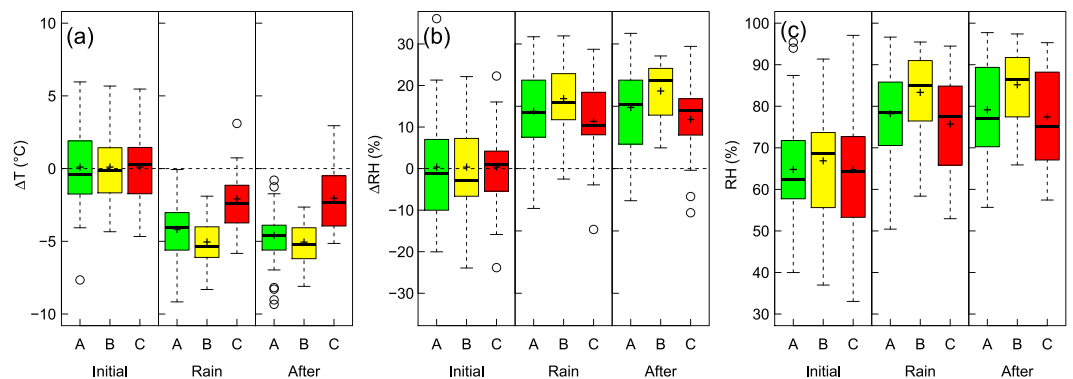


Figure 9. Same as Figure 8 but for (a) changes in surface temperature (°C); (b) changes in relative humidity (%), relative to the mean distribution during the initial stage; and (c) relative humidity (%) during the three stages for each classes (A, in green; B, in yellow; and C, in red) as defined in section 3.2.

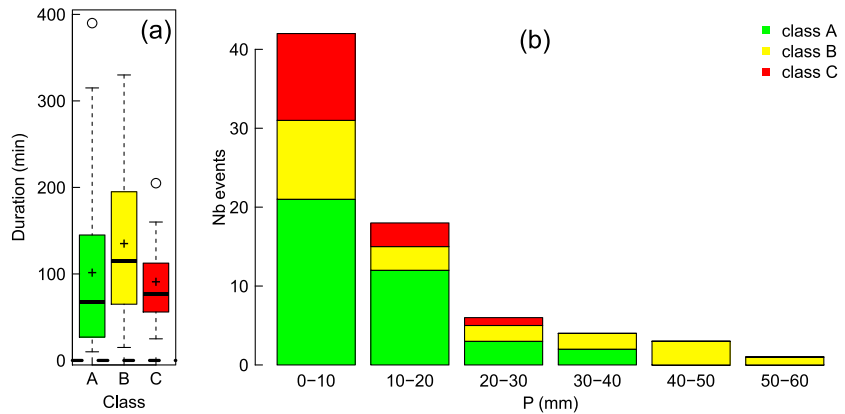


Figure 10. (a) Statistical values (lower and upper quartile, median, spread, and mean represented by black crosses) of rain events duration (min) associated with each class (A, B, and C) as defined in section 3.2. (b) Number of rain events corresponding to each class in function of precipitation amount (mm) recorded by the IRI rain gauge.

This demonstrates that the temporal evolution of the isotopic composition of surface water vapor depends on the type of convection. In particular, the observed decrease in $\delta^{18}O_v$ at the transition between the initial and the rain stage seems to correspond to well-organized convective systems (classes A and B) which bring high precipitation amount like MCS. On the contrary, class C consists of local convective systems which preferentially enrich the water vapor during rainfall. This may be explained by a weaker subsidence and a stronger control of $\delta^{18}O_v$ by rain evaporation in those cases [Risi *et al.*, 2010]. These processes are discussed in

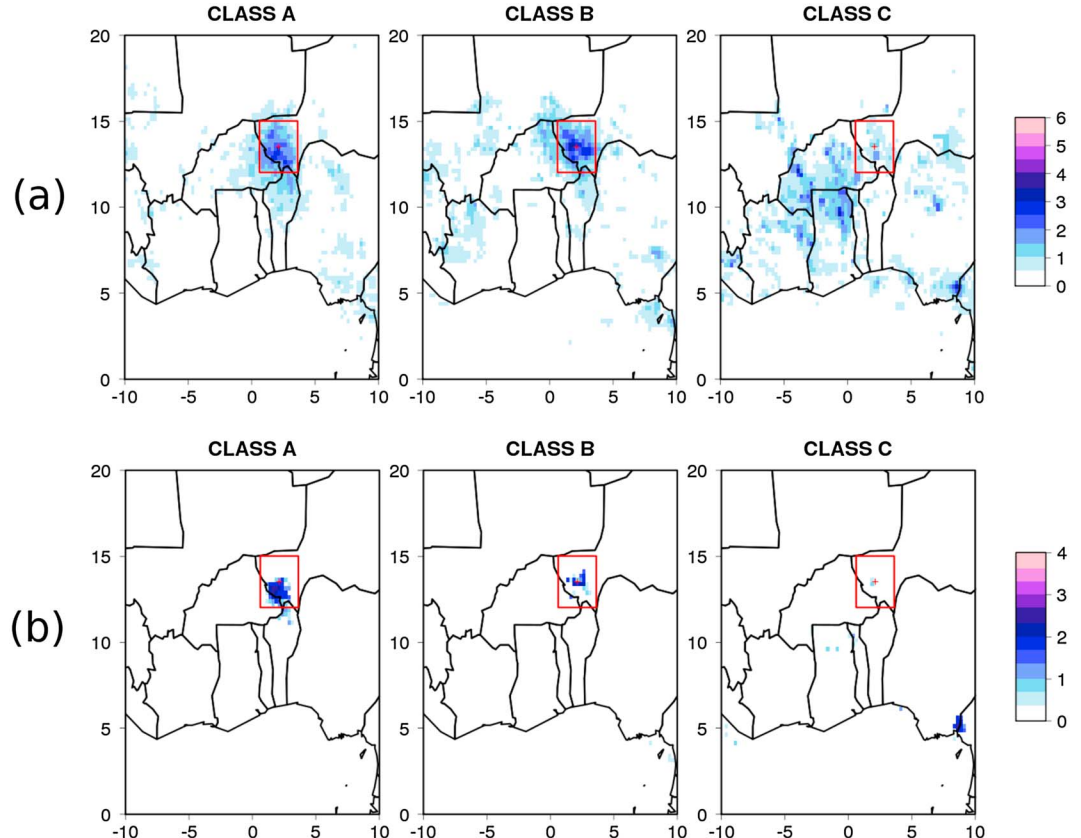


Figure 11. Precipitation rate (mm/h) from TRMM-3B42 during each selected event in function of their class between 10°W–10°E and 0°N–20°N: (a) average and (b) median. Niamey location is indicated by the cross at the center of the 3° × 3° red box.

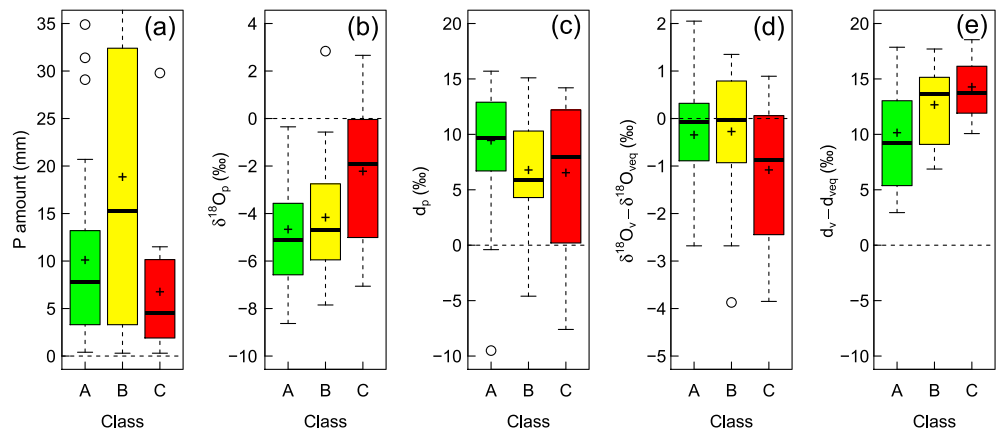


Figure 12. Statistical values (lower and upper quartile, median, and spread, and mean represented by black crosses) for each of the three classes (A, B, and C) as defined in section 3.2 for (a) precipitation amount (mm/event) at IRI (in Niamey), (b) $\delta^{18}O_p$ (‰), (c) d_p (‰), (d) $\delta^{18}O$ disequilibrium between vapor and vapor in equilibrium with precipitation. (e) Same as Figure 12d but for deuterium excess d .

more details in section 3.3. Interestingly, we also observe that, on average, the highest precipitation rates (which occur for class B events) are not associated with the strongest $\delta^{18}O_v$ drops (which occur for class A events, see Figure 8b). This may eventually reflect that the proportion of moisture arising from rain evaporation is more important for class B compared to class A as rain evaporation tends to enrich the vapor [Risi et al., 2010].

3.2.4. Comparison of the Isotopic Composition of Water Vapor and Precipitation

Figures 12b and 12c show the distribution of the isotopic composition of precipitation as a function of the different classes. We clearly observe distinct distributions for each class. Indeed, precipitation is on average more depleted for class A ($\delta^{18}O_p = -4.7 \pm 2.2\text{‰}$) and class B ($\delta^{18}O_p = -4.2 \pm 2.6\text{‰}$) than for class C ($\delta^{18}O_p = -2.3 \pm 3.0\text{‰}$). Interestingly, class A events record highest precipitation deuterium excess ($d_p = 9.3 \pm 5.2\text{‰}$), whereas class B and class C d_p are lower and quite similar on average ($d_p = 6.6 \pm 4.7\text{‰}$ and $d_p = 6.4 \pm 6.9\text{‰}$, respectively) but with different distributions (Figure 12c). This suggests that the isotopic composition of precipitation is more influenced by reevaporation process for classes B and C than for class A, provided that other variables are constant, as evaporation tends to lower d_p at the same time that it increases $\delta^{18}O_p$ (Figure 4).

To confirm this idea, we investigated the difference between the isotopic composition of precipitation and surface water vapor as it brings information on the degree of rain that is reevaporated and diffusive exchanges that take place between falling raindrops and the surrounding water vapor. We estimate for each class the degree of equilibration during the rain stage, through the difference between $\delta^{18}O_v$ and $\delta^{18}O_{v,eq}$ (the isotopic composition of the water vapor theoretically in equilibrium with that of the precipitation). In the ideal case where rain falls into a saturated atmosphere, there is no reevaporation. Precipitation and surface water vapor progress toward isotopic equilibrium through diffusive exchanges between both phases ($\delta^{18}O_v$ tends to $\delta^{18}O_{v,eq}$). On the other hand, when rain falls into unsaturated downdrafts, rain evaporation tends to enrich the precipitation and thus increase $\delta^{18}O_{v,eq}$ compared to $\delta^{18}O_v$ (see also the discussion in section 2.4.4). Thus, the more rain evaporation in the subcloud layer, the more negative $\delta^{18}O_v - \delta^{18}O_{v,eq}$.

We estimated $\delta^{18}O_{v,eq}$ from the isotopic composition of precipitation and the temperature-dependent equilibrium fractionation coefficient α_{eq} between water vapor and precipitation:

$$\delta_{v,eq} = \alpha_{eq} \cdot (\delta_p + 1000) - 1000$$

We calculated α_{eq} using the formulation given by Majoube [1971] and the hypothesis that temperature is the mean temperature between 1000 and 300 hPa, weighted by specific humidity at each vertical level [Tremoy et al., 2012]. To that aim, we used here radio-sounding TEMP data from Niamey airport.

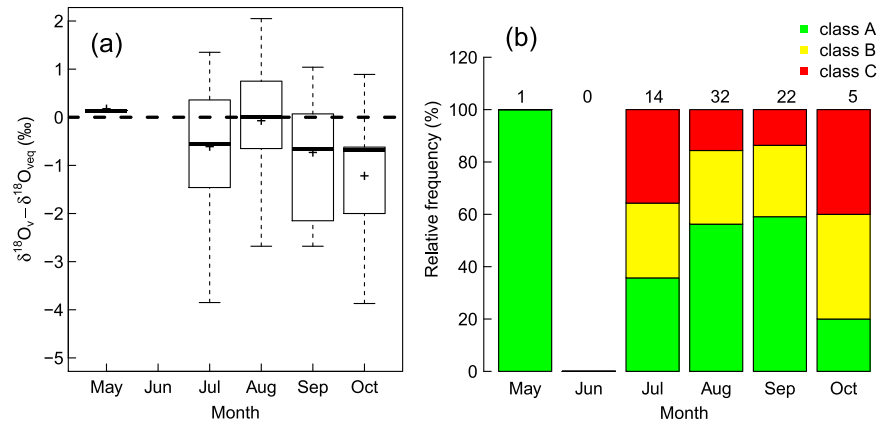


Figure 13. (a) Monthly evolution of $\delta^{18}\text{O}_v - \delta^{18}\text{O}_{v,\text{eq}}$ for all selected events. (b) Monthly evolution of rain events occurrence (%) associated with each class (A, B, and C) as defined in section 3.2 (note that the number n of events is different from month to month and is indicated on top of each bar: $n = 1$, $n = 0$, $n = 14$, $n = 32$, $n = 22$, and $n = 5$ in May, June, July, August, September, and October, respectively; see Table 2).

According to Figure 12d, the distributions of $\delta^{18}\text{O}_v - \delta^{18}\text{O}_{v,\text{eq}}$ are quite similar for classes A and B with a weaker disequilibrium compared to class C ($\delta^{18}\text{O}_v - \delta^{18}\text{O}_{v,\text{eq}} = -0.4 \pm 1.1\text{‰}$, $\delta^{18}\text{O}_v - \delta^{18}\text{O}_{v,\text{eq}} = -0.3 \pm 1.4\text{‰}$, and $\delta^{18}\text{O}_v - \delta^{18}\text{O}_{v,\text{eq}} = -1.1 \pm 1.5\text{‰}$ for classes A, B, and C, respectively). This suggests a strong influence of rain evaporation for class C rain events which is consistent with increasing $\delta^{18}\text{O}_v$ during rain stage (Figure 6). On the contrary, precipitation, and water vapor are generally closer to the equilibrium for classes A and B. Moreover the distributions of $d_v - d_{v,\text{eq}}$ (Figure 12e) considering the 43 rain events selected in 2011 and 2012 are quite consistent with these features. We observe higher differences for class C ($d_v - d_{v,\text{eq}} = 14.1 \pm 4.2\text{‰}$) and class B ($d_v - d_{v,\text{eq}} = 12.5 \pm 3.6\text{‰}$) events compared to class A events ($d_v - d_{v,\text{eq}} = 10.0 \pm 5.8\text{‰}$).

We also observe that the deviation from the equilibrium ($\delta^{18}\text{O}_v - \delta^{18}\text{O}_{v,\text{eq}}$) varies during the monsoon for all the selected events (Figure 13a). Precipitation and water vapor are closer to the equilibrium during the core of the monsoon in August, whereas the difference between $\delta^{18}\text{O}_v$ and $\delta^{18}\text{O}_{v,\text{eq}}$ increases at the beginning and at the end of the rainy season. This behavior is consistent with the monthly evolution of rain event occurrence (Figure 13b) and with the relative humidity of the atmosphere, which is weaker at the beginning and the end of the monsoon season and thus tends to favor rain evaporation at these times.

3.3. Simulations of $\delta^{18}\text{O}$ in MCS

In order to improve our understanding of the meteorological regimes in MCS associated with the different isotopic classes A, B, and C, we compare here the isotopic composition of water between the observations and model outputs. The model is run following the steps described in section 2.4.6. We tuned the model to reproduce at best the observations presented in Figure 7. In this section, we examine the relative contribution of mesoscale subsidence versus rain evaporation, and we discuss the sensitivity to the tuning parameters z^* and ϵ .

Figures 14a and 14b present the model/data comparisons for the 15 August 2011 (class A) and 3 August 2012 (class B) events, respectively. Model/data comparison for class C is not shown since the model fails to reproduce this type of evolution (see section 3.3.3). These figures represent the evolution with time of z^* , f_{rev} along with r_{ev} , the relative and specific humidity as recorded in the observations, and the isotopic composition ($\delta^{18}\text{O}$ and d) of water vapor and precipitation both observed and simulated in the different boxes of the model. The resulting vapor in the wake box is intermediate between the vapor arising from the subsidence box (green dotted line) and the evaporation box (red dotted line) as it results from a mixing of both processes.

3.3.1. Class A Events

Figure 14a shows the results of a simulation applied to the 15 August 2011 rain event. The model reproduces well the $\delta^{18}\text{O}$ observations when z^* varies from 840 hPa at the beginning of the rain stage to 775 hPa at the end, with the assumptions that $\epsilon = 1$ and that $F_{\text{sub}}/F_{\text{up}} = 1$ (see Appendix A). Indeed, the mean $\delta^{18}\text{O}_v$ over

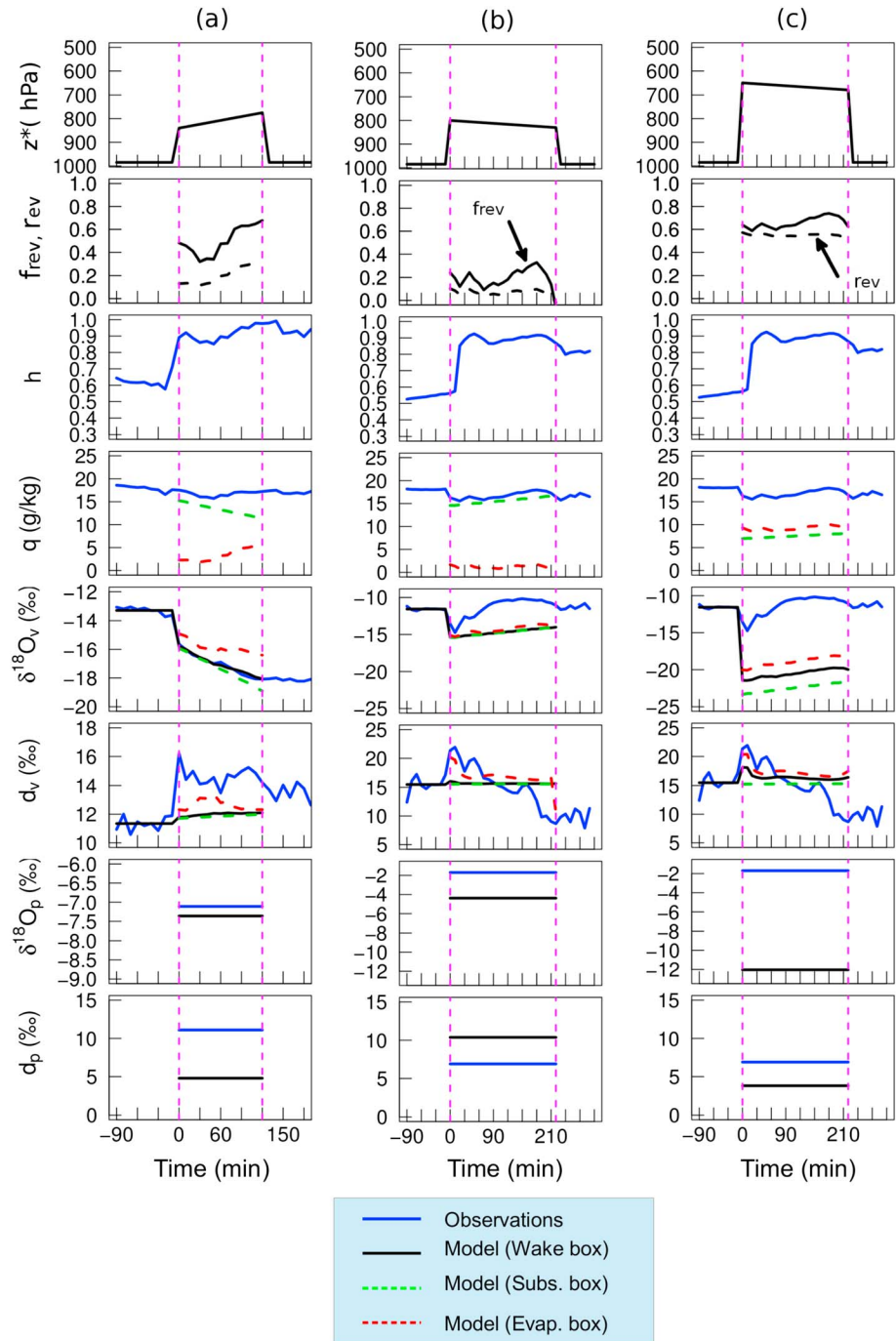


Figure 14. Comparison between data (solid blue lines) and model outputs from the different regions of the MCS (green dotted line for the subsidence box, red dotted line for the evaporation box, and black line for the resulting wake box) considering three different simulations corresponding to (a) 15 August 2011 event (class A) where detrainment height z^* has been fixed between 840 hPa and 775 hPa, (b) 3 August 2012 event (class B) where z^* ranges from 800 hPa to 830 hPa, and (c) 3 August 2012 event (class B) where z^* ranges from 650 hPa to 680 hPa. For these three different simulations, we present the temporal evolution of (from top to bottom): the detrainment height z^* (hPa) where water vapor is transported from the convective to the stratiform part, the fraction f_{rev} of an average droplet that is reevaporated (solid black line) along with the percentage r_{ev} of vapor in the wake box arising from rain evaporation (dashed black line), the observed relative humidity h , the specific humidity q (in g/kg) as observed and simulated in the subsidence box as well as in the evaporation box, the isotopic composition $\delta^{18}O_v$ and d_v (in ‰). The average isotopic composition of precipitation during the storm, $\delta^{18}O_p$ and d_p (in ‰), from the observations and the model are also shown. Dashed vertical lines correspond to rain stage.

the rain stage is $-17.1 \pm 0.8\text{‰}$ and $-17.0 \pm 0.7\text{‰}$ in the observations and the model, respectively. The isotopic composition of precipitation is also well simulated. The difference between observed and modeled event-based $\delta^{18}\text{O}_p$ is 0.3‰ . In those conditions, the simulated r_{ev} ranges from 12% to 34% (Figure 14a). This suggests that for class A, the water vapor in the wake box mostly arises from the subsidence process. The decrease in $\delta^{18}\text{O}_v$ corresponding to the arrival of the wake seems to reflect the previous condensation process that is imprinted in water vapor advected downward by mesoscale subsidence.

Indeed, humidity and isotope ratios in the subsidence box result from the detrainment of convection along the convective column. Since the dynamic mainly advect air from higher levels down to the surface in the stratiform part, the isotopic composition of the water vapor which is transported downward is controlled by the degree of condensation that occurs in the convective zone. The isotopic composition of the advected water vapor is thus dependent on the altitude z^* (it is worth noting that we do not account for the evolution of the isotopic composition of the surface layer that initiates the convection).

For instance, with an initial vapor of $\delta^{18}\text{O}_v = -13.3\text{‰}$, condensation from LCL to $z^* = 775$ hPa leads to a decrease in $\delta^{18}\text{O}_v$ in the subsidence box to -18.9‰ (-17.8‰), and $\delta^{18}\text{O}_p$ from -3.9 to -8.6‰ (-7.5‰) in the case where $\varepsilon = 1$ ($\varepsilon = 0$). Figure 3c shows that $\delta^{18}\text{O}_v$ and $\delta^{18}\text{O}_p$ in the subsidence box are increasingly sensitive to ε as the condensation level z^* increases.

As the air mass becomes dehydrated, the remaining vapor is more and more depleted in heavier isotopologues since they are preferentially redistributed into the condensed phase (equilibrium fractionation). The higher the condensation level, the more depleted the vapor, since isotopic fractionation during condensation is more important at lower temperatures. Thus, water vapor in the subsidence box is more and more depleted as z^* increases from the beginning to the end of the rain stage ($\delta^{18}\text{O}_v^{\text{sub}} = -15.9\text{‰}$ for $z^* = 840$ hPa, whereas $\delta^{18}\text{O}_v^{\text{sub}} = -18.9\text{‰}$ for $z^* = 775$ hPa; see Figure 14a). This sensitivity to cloud top height z^* is also consistent with observations reported from Scholl *et al.* [2009].

If the water vapor recycling by mesoscale subsidence ($1 - r_{ev}$) is on the order of 66% on average during the rain stage in this simulation, the intensity of rain evaporation is significant, in particular at the end of the rain stage (f_{rev} ranges from 32% to 68%). As expected, rain evaporation tends to counterbalance the decreasing effect of subsidence on $\delta^{18}\text{O}_v$ in the wake box. Indeed, the evaporation box tends to enrich the water vapor arising from the subsidence box (see the difference between the green and the red dotted lines in Figure 14a). On average, during the rain stage, $\delta^{18}\text{O}_v^{\text{sub}} = -17.4 \pm 1.0\text{‰}$, whereas $\delta^{18}\text{O}_v^{\text{ev}} = -15.9 \pm 0.5\text{‰}$. Yet the evaporation effect on the vapor simulated in the wake box is increasingly important as the fraction r_{ev} is important along the rain event. Since z^* is weak in this simulation ($z^* < 775$ hPa), the proportion of vapor arising from the evaporation box r_{ev} does not exceed 34% on average. Therefore, q_v^{ev} is weaker than q_v^{sub} ($q_v^{\text{sub}} - q_v^{\text{ev}} = 9.8 \pm 2.6$ g/kg on average during the rain stage). This explains why the simulated isotopic composition of water vapor in the wake box (black curve) is closer to that in the subsidence box (green curve) rather than in the evaporation box (red curve) in this case.

3.3.2. Class B Events

Figure 14b shows the results of a simulation applied to the 3 August 2012 rain event. In this case, z^* ranges from 800 hPa at the beginning of the rain stage to 830 hPa at the end, with the assumptions that $\varepsilon = 1$ and that $F_{\text{sub}}/F_{\text{up}} = 1$. This simulation illustrates the difficulty for the model to reproduce correctly the $\delta^{18}\text{O}$ observations for this type of events. The model fails to reproduce the correct increase in $\delta^{18}\text{O}_v$ during the rain stage.

Similar to class A event (15 August 2011), the drop in $\delta^{18}\text{O}_v$ associated with the beginning of rainfall is well reproduced by the tuning of z^* . However, the progressive increase in $\delta^{18}\text{O}_v$ during the rain stage which follows cannot be purely explained by a decrease in z^* with time. Indeed, z^* values must be higher than the LCL level; otherwise, there is no vapor to detrain in the subsidence box, and consequently, there is no vapor to transport to the wake box by mesoscale subsidence, nor precipitation in the evaporation and wake box. In this simulation, z^* must be higher than 830 hPa. Thus, the possible change in z^* is very weak ($+30$ hPa) and induces an increase in $\delta^{18}\text{O}_v$ of only $+1.4\text{‰}$ between the beginning and the end of rainfall. Therefore, the model underestimates $\delta^{18}\text{O}_v$ by 3.3‰ on average during the rain stage (see Figure 14b). Moreover, the precipitation $\delta^{18}\text{O}$ is also underestimated by 2.7‰ on average during the rain stage. These underestimations suggest that vapor recycling by mesoscale subsidence cannot explain alone the increase in $\delta^{18}\text{O}_v$ which is typical of class B events.

Thus, we suggest that rain evaporation could explain this feature. The intensity of rain evaporation and its contribution to the specific humidity budget in the wake is very weak from the beginning to the end of rainfall ($f_{\text{rev}} = 19 \pm 9\%$ and $r_{\text{ev}} = 7 \pm 3\%$). Thus, the effect of rain evaporation on $\delta^{18}\text{O}_v$ in the wake box is very weak. Figure 14b shows that the simulated $\delta^{18}\text{O}_v$ in the evaporation box (red dotted line) follows the simulated $\delta^{18}\text{O}_v$ in the subsidence box (green dotted line).

This small effect of rain evaporation could be explained by the following reason: z^* values are weak ($z^* < 800$ hPa) which lead to weak values for q^{ev} and thus for r_{ev} (see equations (5) and (7)). Figure 14c presents, for this event, a second simulation where z^* has been shifted by -150 hPa. This change leads to a strong increase in both the proportion of moisture arising from the evaporation box ($r_{\text{ev}} = 55 \pm 1\%$) and the fraction of an average droplet that is reevaporated ($f_{\text{rev}} = 67 \pm 6\%$). Therefore, the rain evaporation effect is stronger compared to the subsidence effect, and the water vapor simulated in the evaporation box is enriched by $+3.5\%$ on average compared to that in the subsidence box (see Figure 14c). However, the shift of z^* also induces a decrease in $\delta^{18}\text{O}$ of both water vapor and precipitation simulated in the subsidence box. As a result, the simulated $\delta^{18}\text{O}_v$ and $\delta^{18}\text{O}_p$ in the wake box are still underestimated compared to the observations.

The difficulty for our model to simulate correctly $\delta^{18}\text{O}$ in the wake box suggests that mesoscale subsidence and rain evaporation are two processes which are not dominant and that other processes exert a major role on the evolution of $\delta^{18}\text{O}$ in MCS. For instance, we suggest that the entrainment of environmental air should be taken into account in the model in order to examine if this process could explain the increase in $\delta^{18}\text{O}_v$ during rain stage. Indeed, *Yoshimura et al.* [2010] studied a rain event similar to class B using a regional model and suggested that moisture convergence contributes to the isotopic enrichment.

3.3.3. Class C Events

For the same reason as class B events, these types of event are not well simulated by our model. These events do not record any depletion of the vapor associated with the beginning of rainfall. Using different values for the tuning parameters of the model, we did not succeed in not simulating a decrease in $\delta^{18}\text{O}_v$. This feature reflects that, in our model, the effect of the subsidence process is always more efficient than the rain evaporation process in controlling the budget of $\delta^{18}\text{O}_v$ in the wake box. Again, this suggests that other processes should be taken into account to improve the representation of reality. In particular, if moisture convergence contributes to an isotopic enrichment [*Yoshimura et al.*, 2010], class C events could reflect strong entrainment rate of environmental air. This result is not in contradiction with a major effect of rain evaporation on the isotopic composition of precipitation as explained in section 3.5 (but other stronger effects contribute to the water vapor isotope ratios).

3.4. Simulations of d Excess in MCS

From Figures 14a–14c, we observe that the model fails to reproduce the evolutions and the mean level of d_v and d_p in the wake box. For instance, the simulation of the class A event underestimates d_v by 2.3% on average during the rain stage. This underestimation can be explained by two possible mechanisms:

1. First, a compensation effect between r_{ev} and f_{rev} . Indeed, r_{ev} depends not only on f_{rev} but also on z^* . In the model, increasing z^* will advect a drier water vapor in the wake and thus will increase the percentage of vapor arising from evaporation r_{ev} and also the fraction of an average droplet that is reevaporated f_{rev} . Therefore, simulated d_v in the evaporation box tends to decrease (Figure 4). Moreover, when z^* becomes lower, q_v^{sub} becomes higher, and q_v^{ev} decreases as well as r_{ev} and f_{rev} . Therefore, simulated d_v in the evaporation box increases (Figure 4), but low r_{ev} explains that simulated d_v in the wake box is not very influenced by rain reevaporation processes.
2. Second, relative humidity, as measured at the surface, might not be representative of the relative humidity at which rain evaporation occurs. Indeed, the d_v increase due to rain evaporation is more efficient when relative humidity is low. Thus, high relative humidity at the surface is partly responsible for the underestimated increase in d_v . To test this hypothesis, we lowered the relative humidity in the evaporation box by 50% compared to the measurements recorded at the surface in the simulation applied to class A event. We also increased z^* so that it ranges from 800 hPa to 700 hPa. This modification of z^* enables us to increase the proportion of moisture arising from rain evaporation r_{ev} . With these modifications, we observe that the increase in d_v between the initial stage and the rain stage is greater by 1% compared to the initial simulation (not shown). We still underestimate the mean increase in d_v , but we match the observations better (1.3% of difference).

3.5. Summary of Simple Model Results

Although we only consider two processes, the model is able to reproduce the main features of the water vapor observations to first order for class A events. Specifically, the depletion of the water vapor is consistent with the fact that z^* increases from the convective to the stratiform part, suggesting that mesoscale subsidence plays a major role along the MCS in feeding surface layer moisture. Similarly, the water vapor depletion recorded at the beginning of rainfall for class B events can be interpreted as the effect of mesoscale subsidence. However, the model fails to reproduce the enrichment of vapor correctly. If the decrease in detrainment height z^* , or the intensification of rain evaporation process, can explain an enrichment of the vapor in the model, this increase remains underestimated. For the same reason, the model fails to reproduce the isotopic evolution of class C events.

One of the objectives of the paper was to test the dominant role of mesoscale subsidence and reevaporation of droplets in controlling the isotopic composition of surface water vapor. Our model confirms this dominant role for 51% of rain events (class A). The mixed results for classes B and C reveal how complex convective systems are: the 1-D model does not resolve explicitly the dynamic structure of a MCS, which prevents us from estimating correctly the different flux of moisture in the convective and stratiform parts of the MCS. The mixed results for classes B and C also reveal that other major controls on the isotopic composition of water vapor may exert a dominant role, strong enough to offset both subsidence and reevaporation of droplets. We cite among them (1) the influence of soil evaporation, which contributes to the re moistening of the low levels and may act like rain evaporation on the isotopic composition of the water vapor; (2) the entrainment of environmental air which can bring moisture with a specific isotopic composition; (3) the evaporation of droplets from ice crystals in mixed phase clouds [Bolot *et al.*, 2013], since we do not take into account the existence of solid particles; and (4) transpiration of water vapor from vegetation. However, taking into account such additional processes requires the use of more elaborated and realistic models, fitted with a convection scheme for instance.

4. Conclusion and Perspectives

4.1. Conclusions

We document here the high-frequency evolution of the near-surface water vapor isotopic composition associated with different rain events in the Sahel region. This region is characterized by intense deep convection and strong rain evaporation processes during the monsoon period. We generally observe three different types of evolution regarding $\delta^{18}\text{O}_v$ (classes A, B, and C).

We demonstrate the potential of these measurements to investigate the role of convective processes and simulate the isotopic evolution of water in MCS using a simple box model. In particular, we quantify the respective roles of mesoscale subsidence and rain evaporation in controlling the proportion of moisture and the isotopic composition of subcloud vapor. We applied this model to the different isotopic classes A, B, and C. The model replicates well the isotopic composition of water vapor for class A; however, it fails to reproduce well the increasing isotopic composition of water vapor occurring during rain stage for classes B and C. This implies that if subsidence and rain evaporation play a dominant role in cold pools on water vapor ratio for class A, other processes must offset the effects of both rain reevaporation and mesoscale subsidence for classes B and C.

We summarize below the main characteristics of each isotopic class, as well as the interpretation of their water isotopic evolution in terms of atmospheric mechanisms:

1. The most frequent type of evolution (class A, 51.35%) corresponds to events where water vapor depletion is strong and dominates during rain stage. Class A events exhibit a depletion in the near-surface water vapor by -1.9‰ for $\delta^{18}\text{O}_v$ on average and an increase in its deuterium excess by 2.3‰ . This category also corresponds to events for which precipitation and vapor composition are the closest to equilibrium, because high relative humidity favors diffusive exchanges between falling droplets and surrounding vapor. Our modeling study demonstrates that for class A events, mesoscale subsidence is the major control of the isotopic composition of surface vapor. The model shows that the recycling of surface vapor by mesoscale subsidence ($1 - r_{ev}$) is on the order of 66% for the simulation of the 15 August 2011 event. Deuterium excess of the vapor first records a sharp increase and then a progressive decrease. The sharp increase may reflect the influence of rain evaporation in the stratiform part below the cloud base,

- where relative humidity is lower than at the surface. The progressive decrease in d_v could be explained by the progressive reequilibration of vapor with precipitation.
2. Class B events (28.38%) correspond to intense convective systems with high precipitation rates. Class B also records depletion of water vapor right after the transition between the initial stage and the rain stage. Unlike class A events, $\delta^{18}\text{O}_v$ increases during rain stage. On average, class B events exhibit a depletion in the near-surface water vapor by -1.2‰ for $\delta^{18}\text{O}_v$ and an increase in its deuterium excess by 1.1‰ . This suggests that more intense convective systems show a stronger rain evaporation effect, weaker reequilibration processes, and stronger entrainment rate of environmental air into the stratiform part of the MCS.
 3. Class C events are the least frequent (20.27%) and usually correspond to small precipitation rates. The particular isotopic signature of water vapor which increases during rain stage (by $+0.8\text{‰}$ for $\delta^{18}\text{O}_v$ on average) seems to indicate a weaker intensity of the mesoscale subsidence as well as a stronger entrainment rate of environmental air into the stratiform part of the MCS. Although our model fails to capture the evolution of $\delta^{18}\text{O}_v$, precipitation is relatively enriched and presents high disequilibrium with water vapor in those cases. This suggests that rain partially evaporates even if this process is not dominant to explain water vapor isotope ratios.

Our study demonstrates that there are other processes besides mesoscale subsidence and rain evaporation which contribute to the control of the isotopic composition of near-surface water vapor. The simultaneous measurements of precipitation and water vapor are essential to improve our understanding of the interactions between both phases.

4.2. Perspectives

We are aware that the temporal evolution of our measurements strongly depends on convective systems spatial stationarity. Having more instrumented sites around Niamey station would allow us to measure several points in latitudinal and longitudinal transects and to go further into these questions. More systematic measurements of the isotopic composition of the rain at high frequency would have been also helpful.

In addition, high-frequency measurements in the middle-to-high troposphere, coupled with surface measurements, would be very helpful to improve our understanding of (1) how air is dehydrated in the convective column by condensation processes and constrain parameters such as ε more precisely (Does the depletion strictly follow a Rayleigh distillation? Are equilibrium processes with cloud droplet or lofted ice important?) and (2) how rain is reevaporated in the various vertical levels in the stratiform part.

Such high-frequency near-surface measurements represent an unprecedented data set to evaluate the representation of convection schemes in numerical models equipped with an isotopic scheme [Risi *et al.*, 2012]. For example, the physics of Laboratoire de Météorologie Dynamique Zoom version (LMDZ) general circulation model, which is fitted with a water isotopes scheme, has been recently improved [Hourdin *et al.*, 2013]. It now includes a new parametrization of the boundary layer, thermals, and a parametrization of cold pools [Rio *et al.*, 2009]. Comparing model simulations with observations would be a first step to evaluate the role of cold pools in the control of the isotopic composition of water vapor in the model. This could also bring information on possible biases related to these processes.

Appendix A: Calculation of f_{rev} and M

The isotopic composition of water vapor and precipitation during rain evaporation depends, among other parameters, on the fraction of an average droplet that is reevaporated f_{rev} [Stewart, 1975]. In the wake box (see section 2.4.5) we begin by calculating the proportion of moisture r_{rev} arising from rain evaporation and the corresponding specific humidity q_{ev} . This enables us to calculate f_{rev} using the following equations.

Considering that the precipitation rate P is proportional to the mass of rain and the convective large-scale flux F_{up}

$$P = F_{\text{up}} \cdot q_p \tag{A1}$$

In a similar way, the evaporation rate E can be expressed as a function of the subsiding flux F_{sub} :

$$E = F_{\text{sub}} \cdot q_{\text{ev}} \tag{A2}$$

We assume that the unsaturated downdraft is in a steady state and that the surface is constant with the altitude.

The evaporation flux can also be expressed as a function of the precipitation rate and f_{rev} :

$$E = f_{\text{rev}} \cdot P \quad (\text{A3})$$

Injecting equations (A1) and (A2) into equation (A3) and writing q_p as a function of ε , $q_p = \varepsilon \cdot (q_v^i - q_{\text{sub}})$, we get the following expression for the fraction of an average droplet that is reevaporated:

$$f_{\text{rev}} = \frac{q_{\text{ev}}}{\varepsilon \cdot \frac{F_{\text{up}}}{F_{\text{sub}}} \cdot (q_v^i - q_{\text{sub}})} \quad (\text{A4})$$

It is important to emphasize that the modification of the isotopic composition of vapor and precipitation during rain evaporation also depends on the relative proportion of initial liquid droplet and water vapor ($M = q_v/q_{p0}$) [see Bony *et al.*, 2008]. For instance, a small amount of rain falling into a big amount of water vapor will have less influence on the isotopic composition of water vapor and especially on its deuterium excess. This initial ratio M can be expressed as follows:

$$M = \frac{F_{\text{sub}} \cdot q_{\text{sub}}}{P} \quad (\text{A5})$$

Using equation (A1) and the definition of q_p , we find

$$M = \frac{F_{\text{sub}}}{F_{\text{up}}} \cdot \frac{q_{\text{sub}}}{\varepsilon \cdot (q_v^i - q_{\text{sub}})} \quad (\text{A6})$$

We assume in section 3.3 of this study that the ratio between large-scale flux $F_{\text{sub}}/F_{\text{up}}$ is constant along rain stage and discuss the sensitivity to ε ($0 < \varepsilon < 1$).

Acknowledgments

We deeply thank Olivier Cattani, Sonia Falourd, and Bénédicte Minster for helping with the isotopic measurements of water vapor and precipitation, Ibrahim Mainassara for taking care of the meteorological measurements at IRI, and Théo Vischel for providing the 5 min rainfall data from Amma-Catch network. We also thank Amaëlle Landais, Anaïs Orsi, Hans Christian Steen-Larsen, James R. Lawrence, and three anonymous reviewers for their very useful comments regarding this paper.

References

- Bolot, M., B. Legras, and J. Moyer (2013), Modelling and interpreting the isotopic composition of water vapour in convective updrafts, *Atmos. Chem. Phys.*, *13*, 7903–7935.
- Bony, S., C. Risi, and F. Vimeux (2008), Influence of convective processes on the isotopic composition ($\delta^{18}\text{O}$ and δD) of precipitation and water vapor in the tropics: 1: Radiative-convective equilibrium and Tropical Ocean-Global Atmosphere-Coupled Ocean-Atmosphere Response Experiment (TOGA-COARE) simulations, *J. Geophys. Res.*, *113*, D19305, doi:10.1029/2008JD009942.
- Caniaux, G., J.-L. Redelsperger, and J.-P. Lafore (1994), A numerical study of the stratiform region of a fast-moving squall line. Part I: General description and water and heat budgets, *J. Atmos. Sci.*, *54*, 2046–2074.
- Chalon, J.-P., G. Jaubert, F. Roux, and J.-P. Lafore (1988), The West African squall line observed on 23 June 1981 during COPT 81: Mesoscale structure and transports, *J. Atmos. Sci.*, *45*, 2744–2763.
- Charba, J. (1974), Application of gravity current model to analysis of squall-line gust front, *Mon. Weather Rev.*, *102*, 140–156.
- Chong, M., and D. Hauser (1989), A tropical squall line observed during COPT 81 experiment in West Africa. Part II: Water budget, *Mon. Weather Rev.*, *117*, 728–744.
- Chong, M., and D. Hauser (1990), A tropical squall line observed during COPT 81 experiment in West Africa. Part III: Heat and moisture budgets, *Mon. Weather Rev.*, *118*, 1696–1706.
- Chong, M., P. Amayenc, G. Scialom, and J. Testud (1987), A tropical squall line observed during COPT81 experiment in West Africa. Part 1: Kinematic structure inferred from dual-doppler radar data, *Mon. Weather Rev.*, *115*, 670–694.
- Dansgaard, W. (1964), Stable isotopes in precipitation, *Tellus*, *16*, 436–468.
- Fontaine, B., and S. Louvet (2006), Sudan-Sahel rainfall onset: Definition of an objective index, types of years, and experimental hindcasts, *J. Geophys. Res.*, *111*, D20103, doi:10.1029/2005JD007019.
- Galewsky, J., C. Rella, Z. Sharp, K. Samuels, and D. Ward (2011), Surface measurements of upper tropospheric water vapor isotopic composition on the Chajnantor Plateau, Chile, *Geophys. Res. Lett.*, *38*, L17803, doi:10.1029/2011GL048557.
- Gedzelman, S. D., and J. R. Lawrence (1990), The isotopic composition of precipitation from two extratropical cyclones, *Mon. Weather Rev.*, *118*, 495–509.
- Hauser, D., F. Roux, and P. Amayenc (1988), Comparison of two methods for retrieval of thermodynamic and microphysical variables from Doppler radar measurements: Application to the case of a tropical squall line, *J. Atmos. Sci.*, *45*, 1285–1303.
- Hourdin, F., *et al.* (2013), LMDZ5B: The atmospheric component of the IPSL climate model with revisited parameterizations for clouds and convection, *Clim. Dyn.*, *40*, 2193–2222.
- Houze, R. A., Jr. (2004), Mesoscale convective systems, *Rev. Geophys.*, *42*, RG4003, doi:10.1029/2004RG000150.
- Huffman, G. J., R. Adler, D. T. Bolvin, G. Gu, E. J. Nelkin, K. P. Bowman, Y. Hong, E. F. Stocker, and D. B. Wolff (2007), The TRMM Multisatellite Precipitation Analysis (TMPA): Quasi-global, multiyear, combined-sensor precipitation estimates at fine scales, *J. Hydrometeorol.*, *8*, 38–55.
- Janowiak, J. E. (1988), An investigation of interannual rainfall variability in Africa, *J. Clim.*, *1*, 240–255.
- Kerstel, E. R. T., R. van Trigt, N. Dam, J. Reuss, and H. A. J. Meijer (1999), Simultaneous determination of the $^2\text{H}/^1\text{H}$, $^{17}\text{O}/^{16}\text{O}$, and $^{18}\text{O}/^{16}\text{O}$ isotope abundance ratios in water by means of laser spectrometry, *Anal. Chem.*, *71*, 5297–5303.
- Kurita, N. (2013), Water isotopic variability in response to mesoscale convective system over the tropical ocean, *J. Geophys. Res. Atmos.*, *118*, 10,376–10,390, doi:10.1002/jgrd.50754.
- Lafore, J. P., and M. Moncrieff (1989), A numerical investigation of the organization and interaction of the convective and stratiform regions of tropical squall lines, *J. Atmos. Sci.*, *46*, 521–544.
- Lafore, J. P., J.-L. Redelsperger, and G. Jaubert (1988), Comparison between a three-dimensional simulation and Doppler radar data of a tropical squall line: Transports of mass, momentum, heat, and moisture, *J. Atmos. Sci.*, *45*, 3483–3500.

- Lawrence, J. R., S. D. Gedzelman, D. Dexheimer, H.-K. Cho, G. D. Carrie, R. Gasparini, C. R. Anderson, K. P. Bowman, and M. I. Biggerstaff (2004), Stable isotopic composition of water vapor in the tropics, *J. Geophys. Res.*, *109*, D06115, doi:10.1029/2003JD004046.
- Lebel, T., et al. (2011), The AMMA field campaigns: Accomplishments and lessons learned, *J. Atmos. Sci.*, *12*, 123–128.
- Lee, X., R. Smith, and J. Williams (2006), Water vapour $^{18}\text{O}/^{16}\text{O}$ isotope ratio in surface air in New England, USA, *Tellus, Ser. B*, *58*, 293–304.
- Liebmann, B., and C. A. Smith (1996), Description of a complete (interpolated) outgoing longwave radiation dataset, *Bull. Am. Meteorol. Soc.*, *77*, 1275–1277.
- Liu, C., and M. Moncrieff (1996), An analytical study of density currents in sheared, stratified fluids including the effects of latent heating, *J. Atmos. Sci.*, *53*, 3302–3312.
- Majoube, M. (1971), Fractionnement en oxygene 18 et en deuterium entre l'eau et sa vapeur, *J. Chim. Phys. Biol.*, *68*, 1423–1436.
- Mathon, V., H. Laurent, and T. Lebel (2002), Mesoscale convective system rainfall in the Sahel, *J. Appl. Meteorol.*, *41*, 1081–1092.
- Merlivat, L., and J. Jouzel (1979), Global climatic interpretation of the deuterium-oxygen 18 relationship for precipitation, *J. Geophys. Res.*, *84*, 5029–5033, doi:10.1029/JC084iC08p05029.
- Moncrieff, M., and C. Liu (1999), Convection initiation by density currents: Role of convergence, shear, and dynamical organization, *Mon. Weather Rev.*, *127*, 2455–2464.
- Noone, D. (2012), Pairing measurements of the water vapor isotope ratio with humidity to deduce atmospheric moistening and dehydration in the tropical mid-troposphere, *J. Clim.*, *25*, 4476–4494.
- Noone, D., et al. (2011), Properties of air mass mixing and humidity in the subtropics from measurements of the D/H isotope ratio of water vapor at the Mauna Loa Observatory, *J. Geophys. Res.*, *116*, D22113, doi:10.1029/2011JD015773.
- Redelsperger, J.-L., and J.-P. Lafore (1988), A three-dimensional simulation of a tropical squall line: Convective organization and thermodynamic vertical transport, *J. Atmos. Sci.*, *45*, 1334–1356.
- Rio, C., F. Hourdin, J.-Y. Grandpeix, and J.-P. Lafore (2009), Shifting the diurnal cycle of parameterized deep convection over land, *Geophys. Res. Lett.*, *36*, L07809, doi:10.1029/2008GL036779.
- Risi, C., S. Bony, F. Vimeux, L. Descroix, I. Boubacar, E. Lebreton, I. Mamadou, and B. Sultan (2008a), What controls the isotopic composition of the African monsoon precipitation? Insights from event-based precipitation collected during the 2006 AMMA field campaign, *Geophys. Res. Lett.*, *35*, L24808, doi:10.1029/2008GL035920.
- Risi, C., S. Bony, and F. Vimeux (2008b), Influence of convective processes on the isotopic composition of precipitation and water vapor in the tropics. Part 2: Physical interpretation of the amount effect, *J. Geophys. Res.*, *113*, D19306, doi:10.1029/2008JD009943.
- Risi, C., S. Bony, F. Vimeux, M. Chong, and L. Descroix (2010), Evolution of the water stable isotopic composition of the rain sampled along Sahelian squall lines, *Q. J. R. Meteorol. Soc.*, *136*, 227–242.
- Risi, C., et al. (2012), Process-evaluation of tropospheric humidity simulated by general circulation models using water vapor isotopologues: 1. Comparison between models and observations, *J. Geophys. Res.*, *117*, D05303, doi:10.1029/2011JD016621.
- Schmidt, M., K. Maseyk, C. Lett, P. Biron, P. Richard, T. Bariac, and U. Seibt (2010), Concentration effects on laser-based $\delta^{18}\text{O}$ and $\delta^2\text{H}$ measurements and implications for the calibration of vapour measurements with liquid standards, *Rapid Commun. Mass Spectrom.*, *24*, 3553–3561.
- Scholl, M. A., J. B. Shanley, J. P. Zegarra, and T. B. Coplen (2009), The stable isotope amount effect: New insights from NEXRAD echo tops, Luquillo Mountains, Puerto Rico, *Water Resour. Res.*, *45*, W12407, doi:10.1029/2008WR007515.
- Stewart, M. K. (1975), Stable isotope fractionation due to evaporation and isotopic exchange of falling waterdrops: Applications to atmospheric processes and evaporation of lakes, *J. Geophys. Res.*, *80*, 1133–1146.
- Taupin, J.-D., and R. Gallaire (1998), Variabilité isotopique à l'échelle infra-événement de quelques épisodes pluvieux dans la région de Niamey, Niger, *C. R. Acad. Sci., Ser. Ila Sci. Terre Planetes*, *326*(7), 493–498.
- Tremoy, G. (2012), Etude de la composition isotopique (deutérium et oxygène 18) de la vapeur d'eau à Niamey (Niger): Vers une meilleure compréhension des processus atmosphériques en Afrique de l'Ouest, PhD thesis, Université de Versailles Saint-Quentin-en-Yvelines.
- Tremoy, G., F. Vimeux, O. Cattani, S. Mayaki, I. Souley, and G. Favreau (2011), Measurements of water vapor isotope ratios with wavelength-scanned cavity ring-down spectroscopy technology: New insights and important caveats for deuterium excess measurements in tropical areas in comparison with isotope-ratio mass spectrometry, *Rapid Commun. Mass Spectrom.*, *25*, 3469–3480.
- Tremoy, G., F. Vimeux, S. Mayaki, I. Souley, O. Cattani, C. Risi, G. Favreau, and M. Oï (2012), A 1-year long $\delta^{18}\text{O}$ record of water vapor in Niamey (Niger) reveals insightful atmospheric processes at different timescales, *Geophys. Res. Lett.*, *39*, L08805, doi:10.1029/2012GL051298.
- Vimeux, F., G. Tremoy, C. Risi, and R. Gallaire (2011), A strong control of the South American SeeSaw on the intra-seasonal variability of the isotopic composition of precipitation in the Bolivian Andes, *Earth Planet. Sci. Lett.*, *307*, 47–58.
- Webster, C. R., and A. J. Heymsfield (2003), Water isotope ratios D/H, $^{18}\text{O}/^{16}\text{O}$, $^{17}\text{O}/^{16}\text{O}$ in and out of clouds map dehydration pathways, *Science*, *302*, 1742.
- Wen, X.-F., S.-C. Zhang, X.-M. Sun, G.-R. Yu, and X. Lee (2010), Water vapor and precipitation isotope ratios in Beijing, China, *J. Geophys. Res.*, *115*, D01103, doi:10.1029/2009JD012408.
- Worden, J., D. Noone, K. Bowman, and the Tropospheric Emission Spectrometer science team & data contributors (2007), Importance of rain evaporation and continental convection in the tropical water cycle, *Nature*, *445*, 528–532, doi:10.1038/nature05508.
- Yoshimura, K., M. Kanamitsu, and M. Dettinger (2010), Regional downscaling for stable water isotopes: A case study of an atmospheric river event, *J. Geophys. Res.*, *115*, D18114, doi:10.1029/2010JD014032.
- Zahiri, E.-P. (2007), Cycle de l'eau des systèmes convectifs ouest-africains: Préparation à l'exploitation des mesures radar Xport dans AMMA par simulations, PhD thesis, Université Paul Sabatier.
- Zipsper, E. J. (1977), Mesoscale and convective-scale downdrafts as distinct components of squall-line structure, *Mon. Weather Rev.*, *105*, 1568–1589.